AN ENGINEERING MODEL FOR PREDICTION OF FORCES IN SFD'S AND EXPERIMENTAL VALIDATION FOR OPERATION WITH ENTRAINMENT

by

Sergio Diaz
Dr. Luis San Andrés

May 1999

TRC-SFD-2-99

EXECUTIVE SUMMARY

Squeeze film dampers (*SFDs*) are effective means to provide damping in rotor-bearing systems. *SFDs* are standard elements in gas turbine engines and commonly used in industrial compressors. Yet, lack of understanding of their operation has confined the design and application of *SFDs* to a costly trial and error process based on prior experience.

The inaccurate modeling of the dynamics of film rupture is the major factor preventing the successful application of analytical models to the reliable prediction of *SFDs* forced performance. Lubricant cavitation models developed for hydrodynamic bearings have been applied by extension to *SFDs*. Yet, the characteristic journal motions within a *SFD* result in the entrapment of air into the oil film, thus producing a bubbly mixture that can not be well represented by available film rupture models.

In the present work, an extensive experimental study establishes qualitatively and –for the first time– quantitatively the differences in behavior for *SFD* operation with lubricant vapor cavitation and with air entrainment. The experiments show that most operating conditions lead to air entrainment and entrapment with a notable degradation of the damper dynamic force performance. The tests thus made apparent the limitation of accepted predictive models. Further experiments manifest the performance of *SFDs* operating with controlled bubbly mixtures. These tests support the modeling of air entrapment as a homogeneous mixture of air and oil and provide a reliable database for analysis validation.

An analytical model based on a *homogeneous* mixture is advanced. Good agreement is obtained between the results of this model and the measurements performed in the *SFD* operating with controlled bubbly mixtures. A complementary analytical model is devised to estimate the amount of air entrained in a typical damper configuration. A balance of the axial through flow and the dynamic fluid volume displaced by the motion of the journal brings forth an equation for calculation of the air/oil volume ratio within the squeeze film. The numerical solution of the Reynolds equation for a bubbly mixture along with the predicted air volume fraction renders promising results for reliable prediction of the force performance of *SFDs* operating with naturally entrained air. The results of the research are of immediate engineering applicability and advance the understanding on a complex problem long ignored in spite of its practical importance.

TABLE OF CONTENTS

LIST OF FIGURES

Page

NOMENCLATURE

A	amplitude of journal motion [m].
a_L	uniform pressure zone extent to the left of maximum film thickness.
a_R	uniform pressure zone extent to the right of maximum film thickness.
$\mathbf{b}$	external body force [N/kg]
C	test *SFD* nominal clearance [0.343 mm].
$\mathbf{D}$	deformation tensor [sec^{-1}].
D	test journal diameter [129.4 mm].
$\frac{D_a}{Dt}$	material derivative respect to phase a.
e	test journal orbit radius or eccentricity [0.216 mm].
f	f_r+if_t, squeeze film force per unit length (at location Z_j) [N/m].
$f_r f_t$	radial and tangential components of squeeze film force per unit length [N/m].
$F_r F_t$	radial and tangential forces [N].
FFT	Fast Fourier Transform.
h	$C+ e\ cos(\omega t)$. Local film thickness [m].
i	$\sqrt{-1}$. Imaginary unit.
$\mathbf{I}$	identity matrix.
L	test *SFD* journal length [31.1 mm].
LPM	liters per minute.
$\dot{m}$	mass flow rate per unit length of film [kg/m].
m_a	density of mass production of constituent a [kg/sec m^3].
n	number of full periods of journal motion.
O_f	offset of journal motion (fit) [m].
P	pressure [Pa].
$\overline{p}$	mean pressure [Pa].
$\widetilde{p}$	dynamic pressure component [Pa].
$P(t)$	period-averaged or instantaneous film pressure at location (Z_j, θ). [Pa].
P_o	discharge pressure (ambient) [Pa].
P_{short}	infinitely short bearing approximation of film pressures [Pa].
P_s	Supply pressure [bar].
P_v	vapor pressure [Pa].
P_∞	pressure far from the bubble [Pa].
P_{corr}	corrected pressure field [Pa].
P_{new}	correction to pressure field computed in current iteration [Pa].
P_{old}	pressure field from previous iteration [Pa].
p-p	peak-to-peak amplitude.
PG	pressure gauge.
PP	displacement sensor.
PT	pressure transducer.
q	volumetric flow rate per unit length of film [m^2/sec].
$\overline{q}$	averaged flow rate per unit length of film [m^2].
Q_{oil}	total oil flow supplied to the damper (liters/min)
R	test journal radius [64.7 mm].

$R_{(t)}$ bubble radius [m].
R_{eq} equilibrium bubble radius [m].
r, t radial and tangential coordinates.
S surface tension [N/m].
SLPM standard liters per minute.
t time [sec].
$\hat{t}$ non-dimensional time.
t_o time of minimum film thickness at 0° [sec].
t_0, t_1 initial and final time of air ingestion portion of the motion cycle [sec].
T $2\pi/\omega$. Journal period of motion [sec].
T_∞ temperature far from the bubble [K].
TT temperature transducer.
u radial velocity (outwards) [m/s].
$\mathbf{v}$ velocity vector [m/sec].
v velocity [m/s].
$\hat{v}$ non-dimensional velocity.
V volume [m^3].
$\overline{V}$ gas volume per unit volume of liquid.
$\mathbf{x}$ position vector [m].
X, Y journal center horizontal and vertical coordinates [m].
x, y, z unwrapped coordinate system.
$\hat{x}, \hat{y}, \hat{z}$ non-dimensional coordinates.
X_j $A.\ cos(\Omega t - \phi) + O$. Journal horizontal displacement (curve fitted) [m].
Z axial coordinate.
Z_j axial location of pressure measurements [mm]. Z_1 (5.16 mm), Z_2 (16.7 mm).
Z_0 inlet *SFD* plane.
Z_3 discharge *SFD* plane.
α relaxation factor.
β angle between squeeze film force and radial direction [rad].
β mixture air volume fraction (air volume/total volume).
β_a mixture phase a volume fraction (phase a volume/mixture volume).
$\tilde{\beta}$ averaged volume fraction.
γ dimensionless parameter for air entrainment.
$\partial h / \partial t$ local time rate of change of the film thickness.
ϕ phase of journal motion [rad].
ϕ attitude angle [rad].
χ mixture quality (air mass/total mixture mass).
η number of bubbles per unit volume of liquid phase [$1/m^3$].
μ lubricant viscosity [Pa sec].
μ_A acoustic viscosity [Pa sec].
μ_E effective liquid viscosity [Pa sec].
μ_T thermal viscosity [Pa sec].
π_a interaction forces between components [N].
ρ density.
ρ_a physical density of phase a.

ρ'_a effective density of phase a.
$\hat{\rho}$ averaged density over one period of motion [kg/m^3].
σ stress tensor.
θ angular location of pressure measurements [rad].
θ angular coordinate in a rotating coordinate frame.
Θ angular coordinate in a fixed coordinate frame.
ν kinematic viscosity [m^2/s^2].
ω journal whirl frequency [rad/sec].
ω_n natural frequency [rad/sec].

subindexes

$_a$ generic phase or constituent of the mixture.
$_c$ bubble conditions at the critical radius.
$_g$ gaseous phase or component.
$_G$ air component in the gaseous phase.
$_L$ liquid component.
$_o$ reference state.
$_\infty$ conditions far from the bubble.

1. INTRODUCTION

Damping is necessary to control excessive steady state vibration amplitudes and rotordynamic instabilities that often appear in turbomachinery and other rotating equipment. Squeeze film dampers (*SFDs*) are virtually the only means to introduce viscous damping to attenuate vibrations and to dissipate energy in rotor-bearing systems. *SFDs* have become a standard device in aircraft gas turbine engines, and are often used as retrofit elements in process compressors to remedy rotordynamic problems.

Conceptually, a *SFD* consists of a thin film of lubricant filling the gap between a stationary housing and a non-rotating journal. The fluid is squeezed out due to the journal whirling motions thus generating hydrodynamic pressures and creating a viscous damping force. Figure 1 depicts a typical configuration of a squeeze film damper. A cylindrical journal is fitted to the outer race of a ball bearing, whose inner race is mounted on a rotating shaft. The arrangement forces the journal to follow the shaft lateral motions while spinning freely. An anti-rotation pin prevents the journal rotation so that the journal whirls squeezing the lubricant film and without the shear drag due to the journal rotation, as in typical hydrodynamic journal bearings. Ideally, the resulting hydrodynamic force acting on the journal is a pure damping force opposing the whirling motion, i.e., no stiffness is developed by the *SFD*. In other configurations, the anti-rotation pin is replaced by an elastic structure, commonly referred as a *squirrel cage*, which provides an easily tunable structural stiffness. In many practical applications, some other type of fluid film bearing, like a plain journal bearing or a tilting pad bearing, substitutes the ball bearing (Zeidan et al., 1996).

The Reynolds lubrication equation for incompressible fluids is hitherto used to predict the pressure field in hydrodynamic bearings, including *SFDs* (Vance, 1988). However, Childs (1993), Walton et al. (1987), Zeidan and Vance (1989a, 1990a) establish that the correlation between theory and experiment is considerably less compelling for dampers than for bearings due to the appearance of dynamic lubricant cavitation. It is customarily assumed that, since an ideal fluid is unable to sustain tension, the lubricant would undergo an instantaneous phase change once the fluid vapor pressure is reached. As a result, a vapor filled cavity interrupting the continuity of the fluid film develops. Numerous physical models address the phenomenon of vapor cavitation with different levels of complexity. Braun and Hendricks (1984), and Ku and Tichy (1990) review these models as applied to the Reynolds equation with boundary conditions defining the onset of cavitation and the full film reformation zone. The simplest model, i.e. the half-Sommerfeld or π-film condition, replaces with a uniform (cavitation) pressure any negative pressure resulting from solution of the Reynolds equation. Next, the Swift-Stieber (or Reynolds) condition enforces a null pressure gradient at the cavitation inception boundary to account for flow continuity. The Floberg and Jakobsson-Floberg-Olsson models account for mass transport across the cavitation zone and allow for the occurrence of subambient pressures within the thin fluid film. These models differ from each other in the assumptions about the path followed by the fluid through the cavitation zone.

Zeidan and Vance (1989b, 1990b,c), Walton, et al. (1987), and Hibner and Bansal (1979) report a different film rupture mechanism in open-ended squeeze film dampers, as it occurs when the relative movement between the *SFD* journal and housing drags air into the film eventually leading to a bubbly mixture. Many authors refer to this phenomenon as gaseous cavitation. However, this term is a misnomer strictly applicable to instances where dissolved gases in the lubricant come out of solution at pressures below the saturation value for the non-condensable gas (air), thus forming a single large bubble. In *SFDs*, as well and in dynamically

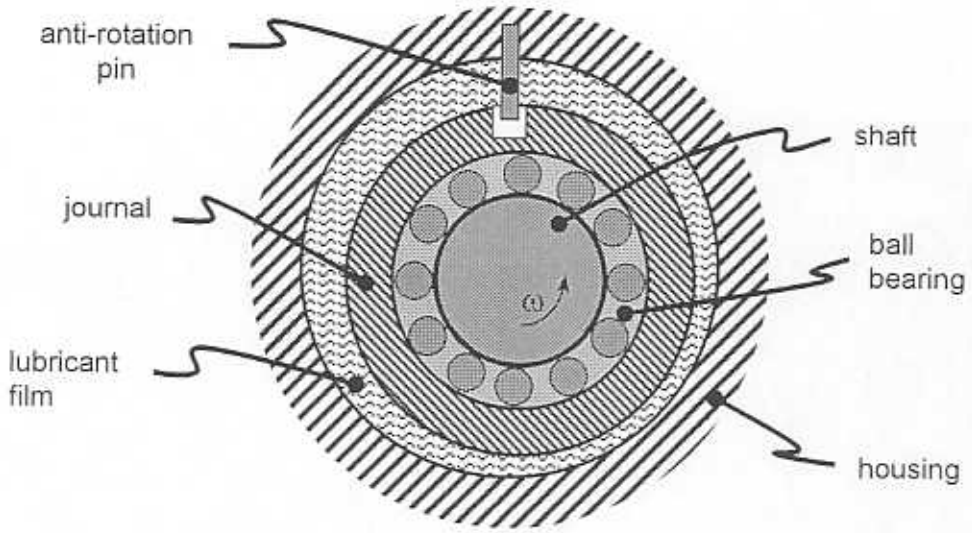

Fig. 1 Sketch of a typical squeeze film damper (SFD) configuration.

loaded journal bearings, the bubbly flow due to air entrainment forms a homogeneous mixture with small bubbles well dispersed throughout the film and persisting even in the high pressure zones. (Dowson and Taylor, 1979, Jacobson and Hamrock, 1983, Zeidan and Vance, 1989a,b, Sun et al., 1993). Foamy oil at the damper outlet evidences this pervasive operating condition.

Zeidan et al. (1996) review the state of the art in *SFDs* and remark about the importance of the air entrainment phenomenon, as it considerably reduces the dynamic film forces and the overall damping capability of *SFDs*. There are no accurate models addressing to the effects of air ingestion in dynamically loaded bearings and *SFDs*, nor are there relevant experimental measurements that could aid in validating predictive analysis. Only recently, Diaz and San Andrés (1998a-c) provide experimental results on a test *SFD* describing circular centered orbits and correlate dynamic pressures and squeeze film forces to the volume concentration of air in a controlled bubbly mixture. The experiments evidence a dramatic reduction in film pressures and forces as the air volume fraction increases in the mixture.

The experimental results hereby presented evidence the paramount effect of air entrainment in the performance of *SFDs* operating with an open-end to ambient discharge, the most common configuration found in practical applications. The measurements show the fundamental differences in film pressure generation and forces for operation with a vented end versus a fully flooded condition where lubricant vaporization prevails. The test results also demonstrate the similarity between the dynamic pressure fields generated by air entrainment and those measured for operation with a controlled homogeneous bubbly mixture. The effect of increased supply pressure and lubricant through flow on the delay of air entrainment within the fluid film is also investigated.

Physical reasoning aided by the praxis gained from the experiments lead to a simple model based on the microscale analysis of the dynamics of a single bubble as described by the *Rayleigh-Plesset* equation. The model renders time-space averaged equations for description of the motion of the lubricant mixture. The end result is a Reynolds-like equation with effective

properties representing a *homogenous* (no relative motion between the components) mixture (Diaz, 1999). Hydrodynamic pressures and forces predicted from the model show good correlation to the experimental measurements of Diaz and San Andrés (1997, 1998a-c) in s damper operating with controlled air in oil mixtures.

The major limitation for the application of the bubbly flow model to actual *SFDs* operating with air entrainment is that the amount of air entrapped in the lubricant film needs to be known a priori. The concentration of air is specified as a reference state for the homogeneous bubbly mixture. A simple model based on the conservation of mass in a control volume is devised for the estimation of the reference mixture volume fraction. The lubricant through flow rate, the geometry of the damper and the kinematics of journal motion define a dimensionless parameter which renders the amount of air entrained into a *SFD* operating with one end open to ambient. This *mixture volume fraction model* is applied in conjunction to the *homogeneous bubbly mixture model* to predict the hydrodynamic pressures and forces in a *SFD* operating with air naturally entrained. The predicted pressures and forces are compared to the experimental measurements and show a significant improvement in relation to prior models.

2. AN EXPERIMENTAL ASSESSMENT OF THE DIFFERENCES BETWEEN LUBRICANT VAPOR CAVITATION AND AIR ENTRAPMENT IN *SFDs*[1]

2.1 Test Rig Description and Experimental Procedures

The experiments are conducted in an open end damper operating with a circular centered whirl orbit of amplitude equal to 50% of the film clearance. Diaz and San Andrés (1998a-c) describe the test apparatus, measurement procedure and uncertainty analysis. Figures 2 and 3 depict the damper test section, flow loop, instrumentation and relevant nomenclature. The damper journal diameter (D) and axial length (L) are equal to 129.4 mm and 31.1 mm, respectively. The journal and its ball bearing are mounted eccentrically on a rigid shaft. A variable speed DC motor and belt transmission drive the shaft supported on two precision ball bearings. At a pressurized condition of 7.0 bar the nominal radial clearance (c) and orbit radius (e) are equal to 0.343 mm and 0.216 mm, respectively. The left end of the damper is tightly sealed with an O-ring, while its right end opens to an exit plenum at ambient pressure. The lubricant enters the damper through two holes at the top (90°) and bottom (270°) of the damper left end.

The experiments are performed with an ISO VG 68 pure lubricant of density and viscosity equal to 0.87 gr/cm^3 and 77.5 centipoise at 28 °C, respectively. The lubricant is delivered to the test section via a gear pump and removed from the discharge plenum with an auxiliary pump. The lubricant flow rate and supply pressure are recorded at the inlet port with a gear flowmeter and a Bourdon type pressure gauge, respectively. A K-type thermocouple detects the lubricant film temperature, a photoelectric tachometer senses the drive shaft speed (equal to the journal whirl frequency), and two eddy current displacement sensors record the motion of the journal. Six piezoelectric dynamic pressure sensors are flush mounted around the damper circumference at two axial planes (Z_1 and Z_2) as depicted in Figures 2and 3.

2.2 Experimental Procedure

The lubricant supply pressure and flow rate, film temperature and synchronous whirl frequency are manually recorded in the experiments. The dynamic film pressure at the location (180°, Z_2), see Figure 2, is measured with a piezoelectric transducer and digitally recorded with 16 bits of resolution at a sampling rate of 2048 Hz for a total length of 2 sec.

Four types of experiments have been conducted to evaluate the performance of the test *SFD* under different operating conditions. Measurements of the pressure field and film forces are performed for fully flooded and open-end vented conditions and for increasing whirl frequencies while maintaining the same supply pressure. In the first type of measurements, the damper discharge plenum is fully flooded with lubricant at atmospheric pressure preventing the ingestion of external air. In this case, the fluid in the damper film lands shows vapor cavitation while the damper operates at a given whirl frequency. The second type of measurements exemplifies a more realistic operating condition where the lubricant discharges to an open plenum vented to atmospheric conditions. In this case air entrains naturally into the squeeze film lands and the discharged lubricant has the appearance of a bubbly mixture resembling a foamy fluid.

---

[1] Adapted from "Air Entrainment vs. Lubricant Cavitation in Squeeze Film Dampers" by Diaz and San Andrés, 1999. *ASME* paper 99-GT-187.

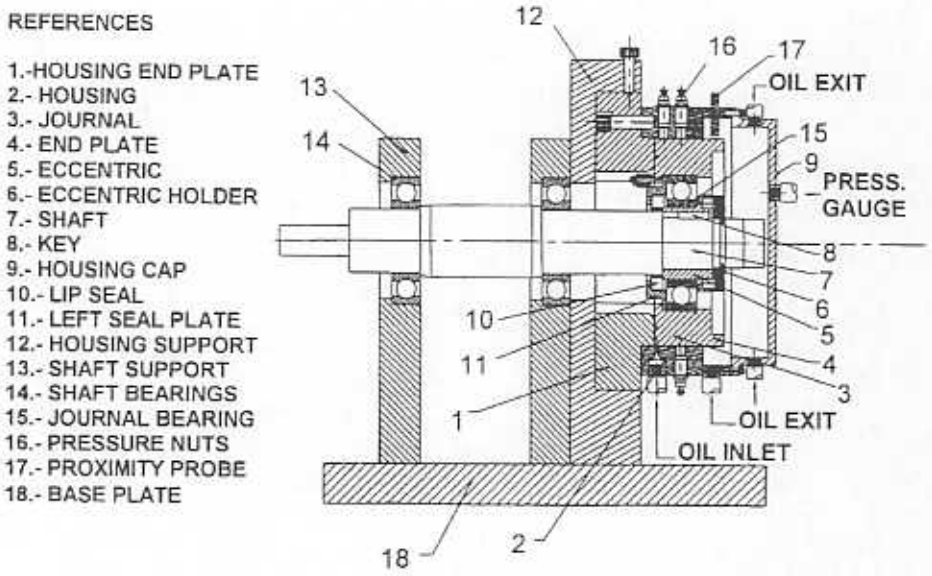

(a) General assembly.

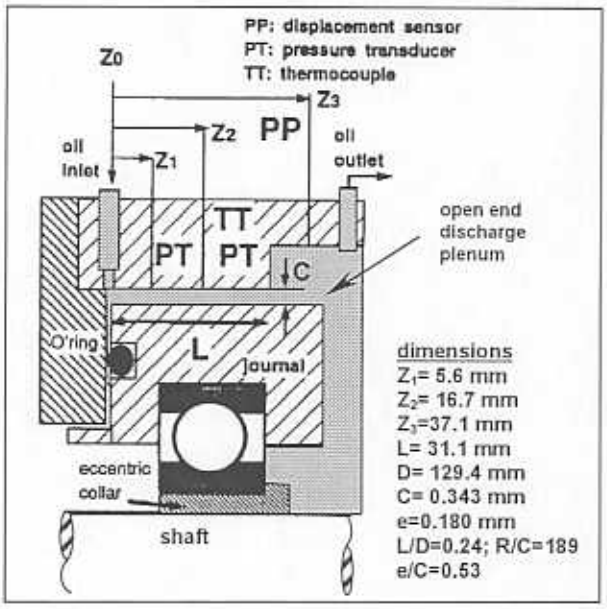

(b) Squeeze film damper detail.

Fig. 2 Squeeze film damper test apparatus.

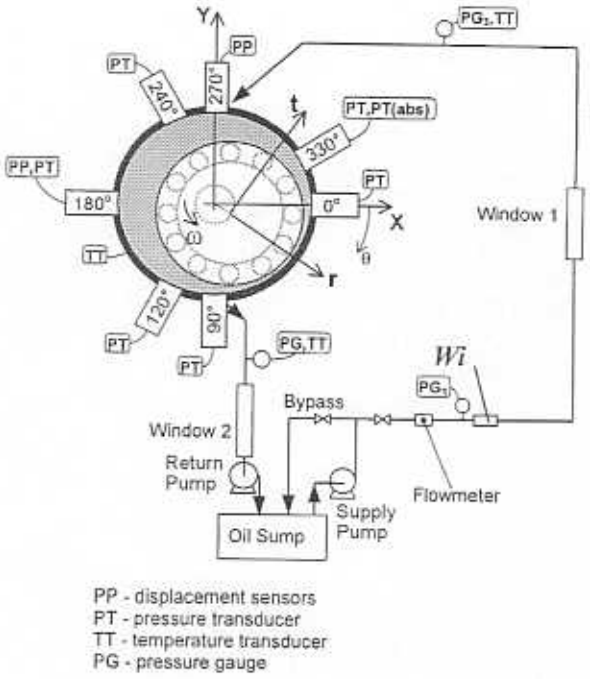

Fig. 3 Schematic view of instrumentation and lubricant lines

In the measurements with increasing whirl frequencies, the supply pressure is set to a constant value of 2.3 bar, which corresponds to a lubricant flow rate of 0.4 l/min. In the vented to ambient condition tests the lubricant is evacuated from the plenum discharge chamber using a small diaphragm pump suctioning at a bottom port. On the other hand, the whole damper test section is submerged in a lubricant bath for the flooded condition tests. In this last case, the lubricant is evacuated from a top port directly to the oil sump. The plenum pressure is at atmospheric pressure for both test conditions. A transparent window on the damper housing discharge section allows verifying that the plenum remains either fully flooded or empty, depending on the type of test conducted. The *SFD* rig is brought rapidly to a maximum shaft speed of 6,000 rpm (100 Hz), and the measurements are performed while reducing the speed by steps of 500 rpm (8.33 Hz) each.

The other two types of measurements illustrate the performance of the open-end vented *SFD* for different lubricant flow rates (pressure supplies) and operating at two whirl frequencies, 8.33 Hz (500 rpm) and 16.67 Hz (1000 rpm). The measurements are performed while the supply pressure (or oil through flow) is increased in discrete steps until the return auxiliary pump is not able to evacuate all the lubricant and the discharge plenum starts to overflow.

The manufacturer values for the uncertainty of the measurement sensors have been verified. The individual errors are 1% of measurement for the oil flowmeter 3% of full scale (10.3 bar) for the Bourdon pressure gauge, and 1% of full scale (100 °C) for the thermocouples. The instrumentation uncertainty on the dynamic pressure measurements is mainly related to the A/D conversion, which is on the order of hundredths of a bar. However, the large temporal fluctuations of the pressures introduce a first-order uncertainty (Moffat, 1982) that overcomes

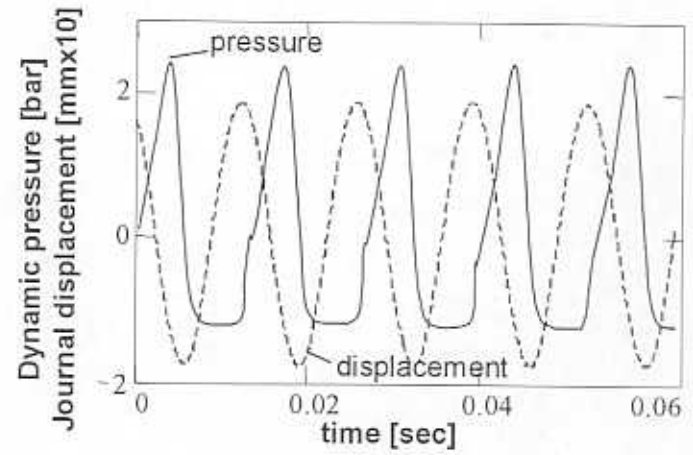

(a) flooded plenum.

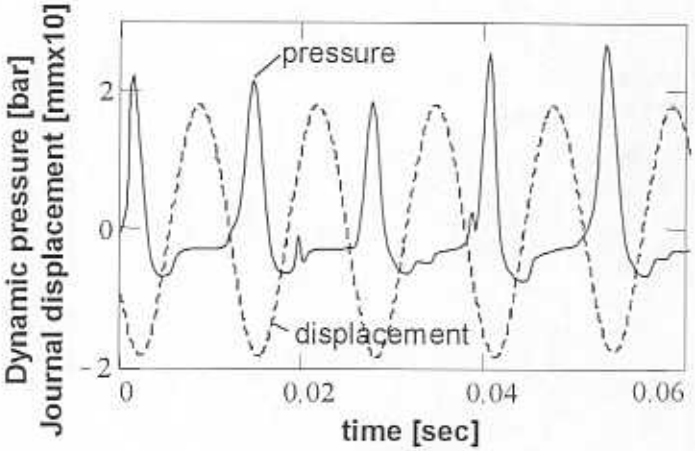

(b) vented plenum.

Fig. 4 Measured dynamic pressures and journal displacements vs time. Flooded and vented plenum.

the instrumentation uncertainty by about two orders of magnitude. The discussion of test results addresses at length this issue.

2.3 Experimental Results

Figure 4 depicts the measured squeeze film pressures for the fully flooded and vented operating conditions. The solid lines represent the dynamic pressures and the dotted lines show the variation of the film thickness at the location of measurement and for five periods of journal whirl motion. In both experiments, the supply pressure is 1.45 bar and the discharge plenum is nearly at atmospheric pressure (1 bar). The oil flow rate is 0.12 liter/min and the film temperature is 27°C. The *SFD* journal describes circular centered orbits with an orbit radius of 0.180 mm at a whirl frequency of 75 Hz.

Figure 4a shows the typical pressure profile found when the pure lubricant undergoes through a vapor cavitation process. The measurements correspond to a piezoelectric dynamic

pressure transducer, thus the negative values in the pressure scale represent pressures below the average pressure and do not mean negative absolute pressures. Note that the pressure profile is smooth and shows nearly identical shapes for each period of motion. A (flat) constant pressure zone develops at nearly zero absolute pressure, and it corresponds to the rupture of the film and formation of a vapor filled cavity. The vapor cavity appears only during that portion of the journal motion period where the film gap increases. The vapor bubble collapses immediately as the local pressure raises above the lubricant vapor pressure. In general, correlations of measured pressures and vapor cavitation extent with predictions based on traditional film rupture models are satisfactory.

The pressure profile shown in Figure 4b shows the effects of air entrainment for the vented to ambient condition. The periodic motion of the journal not only squeezes the lubricant but it also induces air ingestion and entrapment within the film. At the times when the local film gap increases a suction pressure draws air into the thin film and leads to the formation of a bubbly mixture of air in oil, with bubbles persisting even in the high pressure zones. Note that the squeeze film pressures differ markedly for each period of journal motion and even the peak pressures undergo large variations. A pressure flat zone at nearly ambient pressure, typically misnamed as gaseous cavitation zone, initiates when the film goes from its minimum to its maximum values (negative squeeze action). The generation of subambient film pressures is also unique during the negative squeeze portion of the journal motion cycle.

A period averaging scheme is applied to the measured pressures to filter random fluctuations, thus generating smooth periodic pressure fields representative of the overall behavior of the squeeze film pressures over many cycles of motion. Figures 5a and 5b compile the period averaged dynamic pressures corresponding to measurements at different operating whirl frequencies for the flooded and vented open end, respectively. The vertical axis represents the pressure, the horizontal axis depicts the time normalized by the period of motion, and the off-plane axis denotes the whirl frequency ranging from 0 to 100 Hz (0-6,000 rpm). For the flooded condition and at low whirl frequencies the level of external supply pressure prevents the onset of the fluid vapor cavitation zone. However, as the journal whirl frequency increases, the dynamic film pressures are low enough and approach the vaporization pressure, thus initiating the oil vapor cavitation zone. The extent of the vapor cavitation zone increases linearly with the journal whirl frequency.

On the other hand, the dynamic pressures corresponding to operation with a vented discharge condition (Figure 5b) are most distinctive and resemble the pressures measured earlier in the same test rig operating with a controlled homogeneous bubbly mixture of air and oil (Diaz and San Andres, 1998a-c, Diaz, 1999). A constant pressure zone that interrupts the pressure evolution from the minimum to the maximum peak develops and with a magnitude nearly equal to the ambient pressure. The extent of the flat pressure zone increases rapidly with the journal whirl frequency for low frequencies. However as the operating frequency increases further, the extent of the constant pressure zone appears nearly stationary. Diaz and San Andres (1998a,c) have correlated the extent of the constant pressure zone with the concentration of air in a test *SFD* operating with a controlled homogeneous bubbly mixture. Thus, the extent of the flat pressure zone in the current measurements denotes increasing degrees of air entrainment as the whirl frequency increases.

Figure 6 shows a quantitative comparison of the peak-to-peak (*p-p*) pressures generated by the test *SFD* operating with vapor cavitation (flooded plenum) and with air entrapment (vented open end). The magnitude of the *p-p* pressures for the vented condition represents an averaged value from the many periods of measurement. The vertical bars represent the first-order

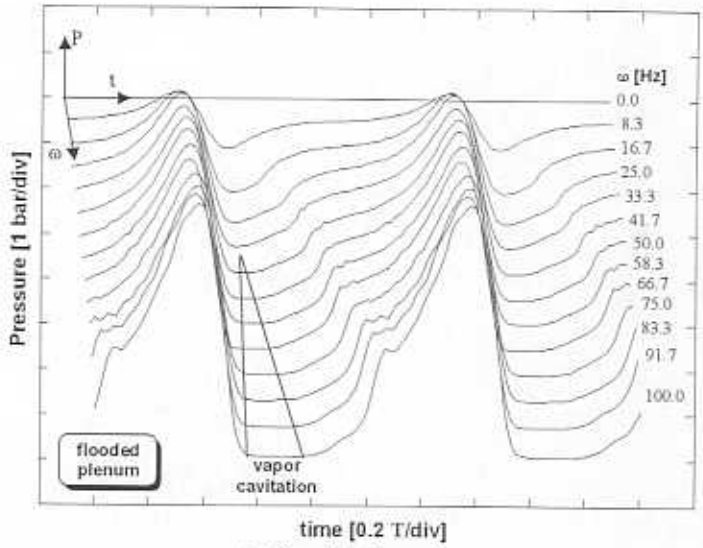

(a) flooded plenum.

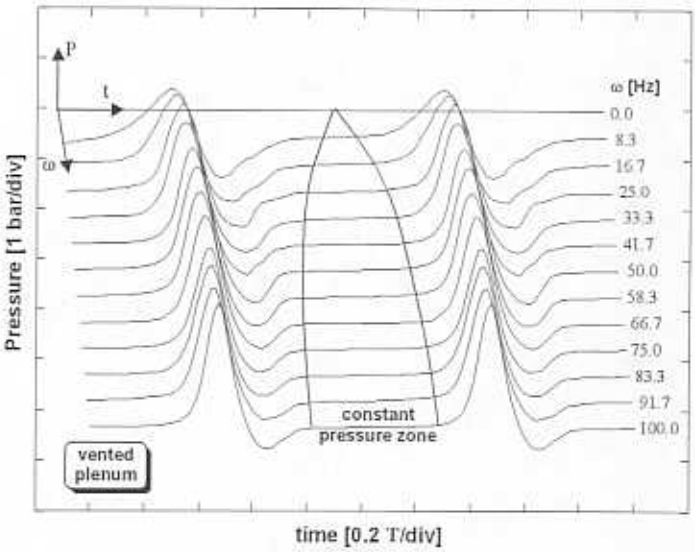

(b) vented plenum.

Fig. 5 Development of the period averaged pressure field and uniform pressure zone vs. whirl frequency (flooded and vented end conditions).

uncertainty as defined by Moffat (1982), i.e. the bars correspond to the largest deviations (above and below) from the average value for the entire length of the experiment. Figure 6 also includes an analytical prediction of the *p-p* pressures and based on the simplest *SFD* model available, the short length bearing with open ends. The pressure is given as

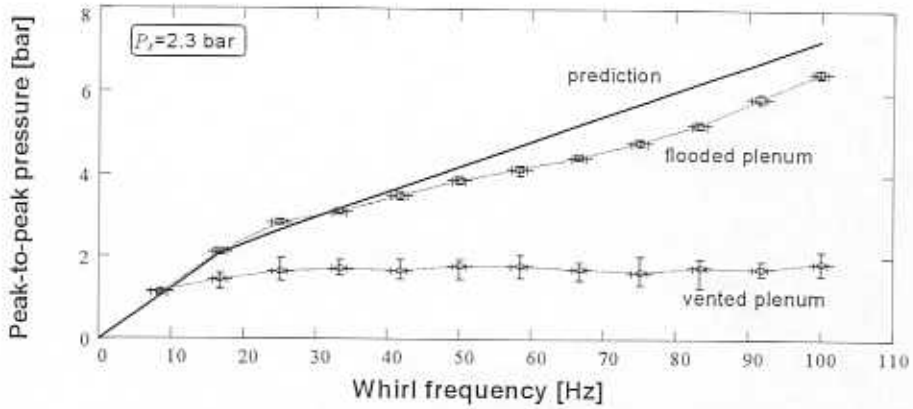

Fig. 6 Peak-to-peak pressure vs. whirl frequency
(flooded and vented end conditions and predictions).

$$P_{short} = \frac{6\mu e\omega}{h^3}\sin(\theta)\left(Z^2 - L^2\right) + P_o \tag{1}$$

and the lubricant vapor cavitation is accounted for with the simple relation,

$$P = \begin{cases} P_{short} & if \quad P_{short} > 0 \\ 0 & if \quad P_{short} \le 0 \end{cases} \tag{2}$$

Refer to the *Nomenclature* for a proper definition of all variables.

The short length bearing model predicts a linear growth of the *p-p* pressures with the journal whirl frequency. The rate of *p-p* pressure raise reduces above the whirl frequency at which the lubricant vapor cavitation initiates (~17 Hz). The experimental pressures for the flooded *SFD* condition correlate very well with the predicted values. However, the p-p pressures for the vented condition quickly reach a constant value, (nearly) independent of the whirl frequency and much lower than for the flooded condition. The first order uncertainties for the flooded condition are rather small indicating a stationary pressure field. On the other hand, the tests with air ingestion and entrapment lead to *p-p* pressure fluctuations of up to 35%.

A *SFD* describing circular centered orbits and with a *stationary*[2] pressure field (synchronous with the shaft) generates invariant forces in a radial and tangential coordinate system rotating with the same speed as the shaft. A pure tangential force is distinctive of an ideal viscous *SFD* since this force directly opposes any forward whirl motion. Radial forces could be centering denoting a stiffness-like effect, or outwards implying a fluid inertia effect. Dynamic damper forces (f_r, f_t) in the radial and tangential directions arise from integration of the pressure field around the journal surface. A kinematic relation between the *stationary* (though rotating) pressure field and the *dynamic* pressure field at a fixed location is used to transform the spatial integration around the journal circumference into integration in time. The relationship is,

[2] Here the stationary qualification means an invariant pressure field relative to an observer positioned in the spinning shaft.

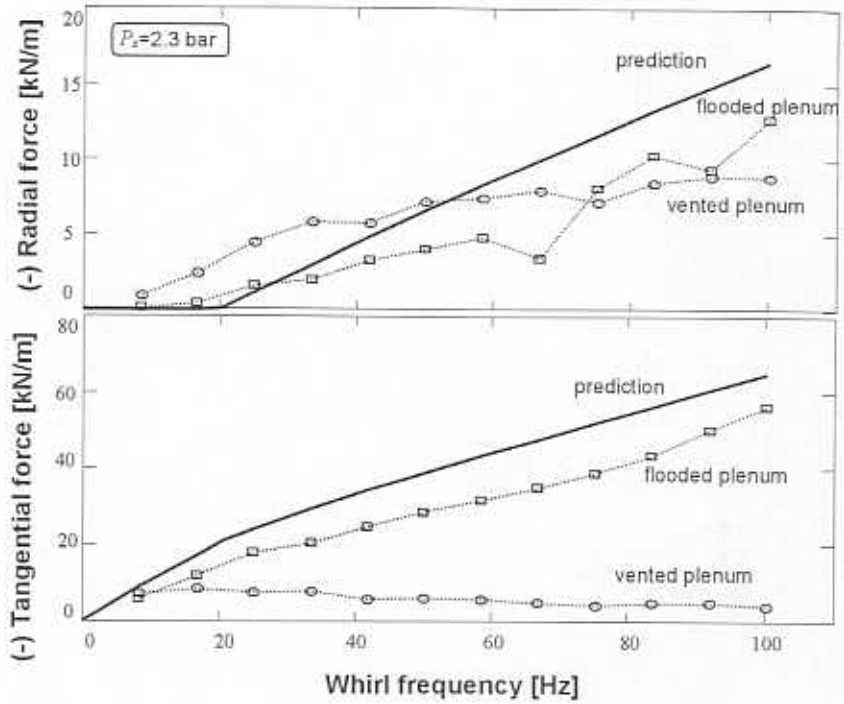

Fig. 7 Radial and tangential forces versus whirl frequency (flooded and vented end conditions and predictions).

$$f_{(Z)} = \left(f_r + i \cdot f_t\right)_{(Z)} = \frac{-\omega \frac{D}{2}}{n} \cdot \int_{t_o}^{t_o + n \cdot T} P_{(t,Z)} \cdot e^{-i \cdot \left[\omega \left(t - t_o\right)\right]} \, dt \tag{3}$$

Refer to the *Nomenclature* for a proper definition of all variables.

Figure 7 depicts the radial and tangential forces per unit length at the axial location of measurement (Z_2) versus the journal whirl frequency. Circles and squares denote the measured forces for the vented and flooded conditions, respectively, and solid lines represent the forces predicted by the short length bearing model. Note that the radial forces are much lower (about 25%) than the tangential (damping) forces and depicted with a different scale. The analytical predictions show the damping force to increase linearly with the whirl frequency, although with a reduced slope after vapor cavitation initiates. The calculated radial force is nil for a full film condition, and increases linearly with the whirl frequency after vapor cavitation initiates. The predictions agree well with the forces derived from the experimental pressures under a flooded discharge operating condition (±10%). Conversely, for the vented plenum and where air entrains naturally into the fluid film, the damping (tangential) force actually decreases as the whirl frequency increases and becomes a mere fraction (15%) of the damping force obtained for the flooded *SFD* condition. At large whirl frequencies when air entrainment is more severe; the radial force becomes larger than the tangential force. Note that for the

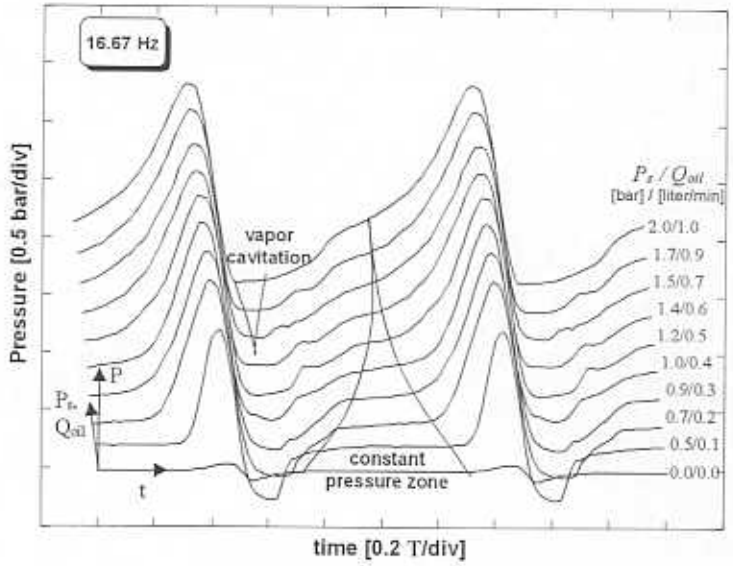

(a) whirl frequency 16.67 Hz (1,000 rpm).

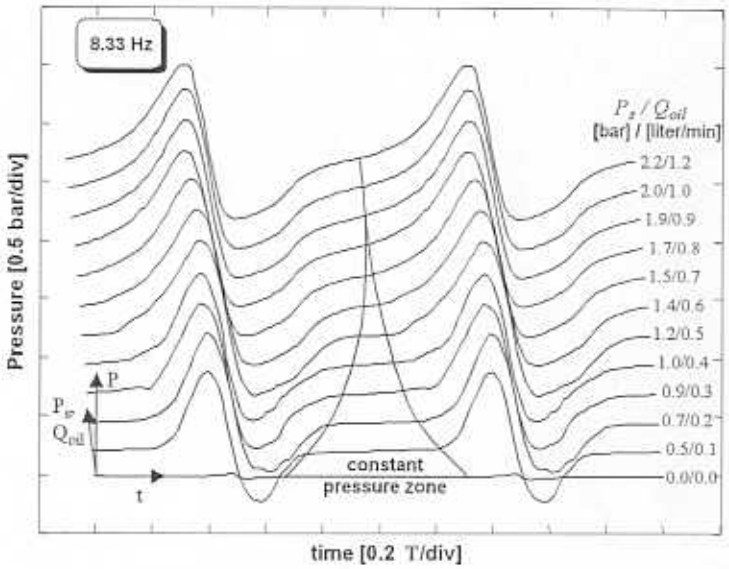

(b) whirl frequency 8.33 Hz (500 rpm).

Fig. 8 Development of the period averaged pressure field and uniform pressure zone vs. the lubricant flow and supply pressure.

computation of the forces it has been assumed that the pressure profile rotates synchronously with the shaft independently of the amount of ingested air in the lubricant. This assumption needs to be verified experimentally.

Figure 8 demonstrates the effects of the supply pressure (lubricant flow rate) on the generation of film pressures and the onset of air entrainment. Figure 8a compiles the period averaged pressures at an operating frequency equal to 16.67 Hz (1000 rpm), and Figure 8b

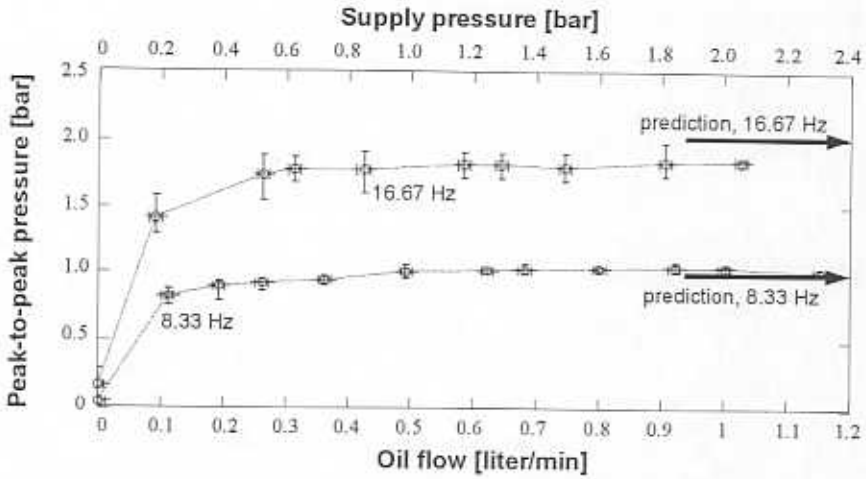

Fig. 9 Peak-to-peak pressures versus oil flow rate and supply pressure for two whirl frequencies.

depicts the pressures at 8.33 Hz (500 rpm). The *SFD* discharge plenum is vented to atmospheric pressure. In the figures, the vertical axis represents the pressure, the horizontal axis depicts the time normalized by the period of motion, and the in-plane axis gives the magnitude of supply pressure and lubricant flow rate. The experiments show that increasing the lubricant through flow rate reduces the extent of the constant pressure zone where air is entrapped. That is, the severity of air entrainment decreases allowing for the generation of larger squeeze film pressures and fluid film forces. Note that in the experiments at 16.67 Hz, a lubricant vapor cavitation zone starts to develop for the largest flow rates.

Figure 9 depicts the period averaged *p-p* pressures corresponding to the dynamic pressures shown in Figure 9 versus the oil flow rate and the supply pressure. The figure also includes the predicted theoretical values derived from the short length bearing model given by equation (1). For both operating whirl frequencies, the *p-p* pressure grows rapidly with the supply pressure. For large flow rates the *p-p* pressures approach an asymptotic value, and correlate well with the simple analytical values. Note that the theoretical model does not predict fluid vaporization or air entrainment at these low frequencies. The experiments also evidence that larger lubricant flow rates are needed to control air entrainment as the whirl frequency increases.

Figure 10 depicts the test radial and tangential forces versus the oil flow rate and supply pressure for the whirl frequencies equal to 8.33 and 16.67 Hz, respectively. Note that, since the radial forces are smaller than the tangential forces, the scales are different on each figure. The experiments at the lower whirl frequency reveal a rapid increase of the tangential film force towards the analytical asymptotic value. However, at the whirl frequency of 16.67 Hz, the tangential (damping) force grows continuously within the full range of test pressure supplies. Unfortunately, the current test facility does not allow for higher levels of pressurization so it is not possible to confirm the asymptotic trend of the tangential force for large flow rates. The radial forces are small and tend to decrease with the supply pressure for the higher test whirl frequency (16.67 Hz). Note that in practice, higher supply pressures are not readily available nor are desired because of the increased operating cost and associated bulky hardware.

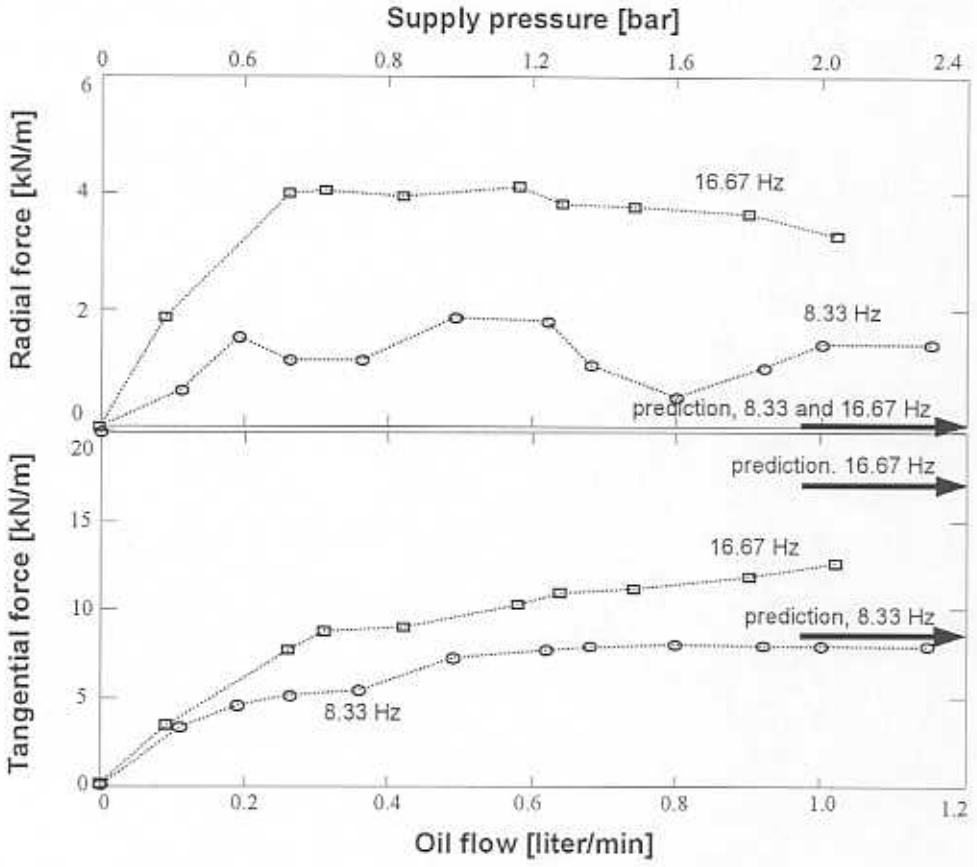

Fig. 10 Radial and tangential forces versus oil flow rate (supply pressure) for two whirl frequencies.

2.4 Summary

The force response of squeeze film dampers is affected by numerous factors, including geometric characteristics, lubricant type, whirl frequency, and supply and discharge mechanisms. Ingestion and entrapment of air is pervasive in *SFDs* operating with vented open ends at ambient pressure. The fluid film becomes a foamy-like mixture with air bubbles persisting in the regions of pressure generation above ambient. Current models for the rupture of thin films, gaseous and vapor cavitation, are strictly applicable for static loads, and their extension to transient or periodic loads gives accurate predictions only for bearings fully submerged in a lubricant bath.

Experiments have been conducted on a controlled orbit test *SFD* operating with two end conditions, one is fully flooded with lubricant, and the other one is just an open vent to ambient as most typical applications exemplify. Measurements of the dynamic film pressures and estimated fluid film forces are performed for increasing whirl frequencies at a fixed value of supply pressure. In the flooded *SFD* the film pressures are quasi-stationary and repetitive for each cycle of damper motion, and where the lubricant vapor cavitation zone increases linearly

with the journal whirl frequency. On the other hand, for the vented condition, and as soon as air is ingested into the film lands, the film pressures show random variations and sudden spikes, zone of subambient pressures, and a discharge fluid appearing as a bubbly mixture. A constant pressure zone at ambient pressure also grows linearly with the whirl frequency.

Period averaged peak-to-peak (*p-p*) pressures and film forces are calculated from the measured pressure fields. For the flooded condition, the *p-p* pressure increases linearly with the journal whirl frequency, and its raise rate reduces at the frequency where lubricant vapor cavitation initiates. The damping (tangential) force shows a similar trend. A radial (centering) force also appears when the fluid vaporizes (cavitation) and its magnitude is proportional to the whirl frequency. In contrast, with a vented plenum condition, the *p-p* pressures quickly reach a constant value, (nearly) independent of the journal whirl frequency and much lower than for the flooded condition. The damping force actually decreases as the whirl frequency increases, and becomes a mere fraction (~15%) of the tangential force obtained from the flooded condition. At large whirl frequencies when air entrainment is more severe; the radial force becomes larger than the tangential force. Theoretical predictions based on a classical model predict well the pressures and forces for the flooded condition (vapor cavitation), but fail to reproduce the test values for the vented condition which develops into a foamy-like mixture. It is important to note that further experiments should be performed to verify that operation with air entrainment still results in a rotating pressure field.

Further experiments at low whirl frequencies demonstrate that increasing the supply pressure reduces the extent of air entrainment and increases the film *p-p* pressures and damping forces. However, the beneficial effect of external pressurization becomes less pronounced as the frequency of operation increases. A sound theoretical model accounting for air entrainment is needed for the reliable design of *SFDs*, thus reducing their costly trial and error tuning process. The test results suggest that considering the squeeze film flow as a homogeneous continuous mixture could lead to an improved predictive analysis.

3. THEORETICAL MODELING OF THE BUBBLY FLOW IN A *SFD*

The previous sections discuss the propensity of squeeze film dampers to develop an operating regime in which air entrapment persists. The measurements demonstrate the paramount effect of air entrapment on the *SFD* force performance. The experimental results also evidence the limitations of the currently available models for prediction of hydrodynamic forces in *SFDs*. These models assume, as in hydrodynamic journal bearings, that *SFDs* develop either vapor cavitation or a single steady bubble of gaseous cavitation. It becomes clear that a reliable mathematical model addressing the operation of *SFDs* with air entrapment is imperative. In this case, the experimental results bolster the possibility of modeling the lubricant as a homogeneous mixture of small air bubbles dispersed in an oil matrix. Furthermore, the experimental results of Diaz and San Andrés (1996, 1997, 1998 a-c) provide a dependable database for validation of models based on this premise.

Two general approaches to the theoretical formulation of bubbly flow in squeeze film dampers are proposed. The first model, developed by Tao et al. (1998)[3], is based on the general methodology of the *Continuum Theory of Mixtures (CMT)*. The formulation considers the oil as an incompressible Newtonian fluid and the air as an ideal gas, both occupying the whole flow domain as a homogeneous field where each material point in space contains particles of both components in a given (not necessarily constant) proportion (Principle of Equipresence). The two components regarded in thermodynamic equilibrium at all times, move with the same velocity field (i.e., no relative motion between the two components). The fluid film is considered isothermal and the effects of the lubricant surface tension are neglected.

Averaged momentum and continuity equations for each component are developed to obtain a differential equation akin to the Reynolds lubrication equation for the mixture pressure along with a relation between the mixture pressure and the local air volume fraction (or mixture density). Unlike the case of a pure lubricant where the specification of boundary conditions for pressure is sufficient, boundary conditions on the volume fraction also need to be specified for a mixture lubricated *SFD*. This additional boundary condition allows the stipulation of different amounts of entrained air or lubricant air volume fraction in the model.

The mixture effective viscosity is no longer a material property as in a pure Newtonian fluid. It can be understood as a statistical parameter affected by the distribution of the two components within the mixture and the characteristics of the flow. Therefore, a numerical correlation to compute the mixture viscosity as a function of the local volume fraction must be determined from careful experimentation. A control-volume (finite difference) scheme is employed to solve iteratively the flow equation for the pressure coupled to the volume fraction and viscosity relations. Numerical integration of the calculated pressures renders the dynamic forces, radial and tangential, acting on the damper journal.

The second model hereby proposed assumes the bubbly mixture to be *homogeneous*, i.e. the gaseous phase is so finely dispersed within the oil that no appreciable relative motion occurs between the phases. Under this assumption, the flow equations for the mixture reduce to the linear momentum equations of a single continuum with some effective physical properties. Therefore, following the typical assumptions of classical lubrication (thin film, laminar flow and no fluid inertia), a general form of the compressible-fluid Reynolds lubrication equation

---

[3] Concurrent research work at the TAMU Tribology Group.

arises for computation of the squeeze film pressures, provided the effective density and viscosity of the mixture are known.

The air/oil mass (quality) ratio is assumed to remain constant in both time and space. Lubricant vaporization/condensation is taken into account by considering the bubbles to be filled with a mixture of air and saturated oil vapor (both assumed as ideal gases). As a result, a constant number of bubbles is fixed per unit mass of liquid (or unit volume if the mass of oil vapor exchanged is considered negligible with respect to the total oil mass). Since the diffusion time required to dissolve an air bubble in oil is relatively high (Sun and Brewe, 1992), the mass of air contained within each bubble is considered invariant and its partial pressure is related to the bubble volume through the ideal gas law. On the other hand, oil vaporization and condensation can be considered instantaneous, and thus the oil vapor is assumed to be in thermodynamic equilibrium with the surrounding oil at all times and with a partial pressure always equal to the vapor pressure of the oil at the mixture temperature.

The size of a single gas/vapor bubble immersed within an infinite incompressible liquid depends on the pressure and temperature of the liquid medium and is governed by the *Rayleigh-Plesset* equation (*RPE*), a second order non-linear differential equation that describes the motion of the bubble surface (Brennen, 1995). The *Rayleigh-Plesset* model represents the momentum equations in polar coordinates applied to the liquid surrounding the bubble (regarded as infinite, incompressible and Newtonian) and coupled with the state equations of the gases inside the bubble. If the interaction among adjacent bubbles is neglected, and further it is assumed that the size of each bubble in the mixture is governed by the *RPE*, then the liquid pressure and temperature are identified at the local mixture conditions. That is, the local density of the mixture can be determined by solving the *RPE* equation. A more complete discussion on the limitations of this assumption follows later.

In its more general form, the *Rayleigh-Plesset* equation includes the effects of surface tension, liquid viscosity, fluid inertia, non-spherical shapes, temperature, change of phase, and many others. However, the model proposed here employs a quasi-static version of the *RPE* on which the characteristic frequency of pressure variation is considered low with respect to the bubble's natural frequency. The assumption produces negligible time derivatives and renders equilibrium between the two phases at all times. The resulting model is a non-linear algebraic equation that relates directly the bubble size to the local mixture pressure. The bubble size distribution renders the volume fraction, which in turn yields the density of the mixture. Note, however, that even when the excitation frequencies are small with respect to the linearized bubble natural frequency for the mean bubble radius, the nonlinearities of the *RPE* could lead to conditions in which the dynamic terms are not negligible. On one side, the natural frequency is a function of the bubble radius, which itself changes in time. On the other hand, when the pressure drops the bubble could reach an unstable condition, i.e. the bubble could grow indefinitely at a rate determined by the dynamic terms of the *RPE*. These possibilities are excluded from the present model, yet it is acknowledged that further analysis is required on this subject. One of the available empirical correlations (such as Cicitti's or Isbin's) is used to evaluate the effective mixture viscosity as a function of the volume fraction. Hence, the effective mixture density and viscosity are represented as functions of the mixture local pressure, providing a closure to the Reynolds equation.

The Reynolds equation for the film pressure, coupled with the effective density and viscosity correlations, is solved iteratively for air/oil mass fractions ranging from zero to one (corresponding to the reference air volume fractions from the experiments). The results are compared with the experimental measurements of Diaz and San Andrés (1997, 1998a-c) in

terms of pressure profiles, peak-to-peak pressures and dynamic forces as a function of the air volume fraction in the mixture.

A final discussion addresses possible refinements to the models and alternative approaches not contemplated in the present work. Expected results and difficulties are pointed out and discussed in light of the experimental results and developed models.

3.1 A Homogeneous Bubbly Mixture Model for *SFDs*

A large number of bubbles are well dispersed throughout the thin film in the presence of air entrapment (Diaz and San Andrés, 1997, 1998a-c). The air bubbles may be of sizes comparable to the film thickness, yet small in comparison to the film axial length and its circumference. The bubbles remain in the film for several cycles of journal motion and survive while passing through high pressure zones. The persistence of these bubbles greatly affects the hydrodynamic pressure generation in the squeeze film. Thus, it becomes necessary to account for the effect of the bubbles in the flow of the lubricant. The observed characteristics of the flow suggest the applicability of the homogenous mixture analysis to describe the hydrodynamics of the lubricant within the film. As stated earlier, when the relative motion between the two phases of the mixture is negligible the governing equations take a form similar to that of a homogeneous single component fluid:

$$\frac{\partial \rho}{\partial t} + \nabla \cdot (\rho \mathbf{v}) = 0 \tag{4}$$

$$\frac{\partial}{\partial t}(\rho \mathbf{v}) + \nabla \cdot (\rho \mathbf{v}\mathbf{v}) = \nabla \cdot \sigma + \rho \cdot \mathbf{b} \tag{5}$$

where $\rho = (1-\beta)\rho_L$ is the effective mixture density.

According to the experimental observations of Diaz and San Andrés (1997, 1998), the flow in the *SFD* film lands can be considered isothermal. Thus, the energy transport equation does not need to be included in the analysis since the lubricant material viscosity is fixed for a constant temperature.

The gas volume fraction, β, is computed from the solution of the isothermal *Rayleigh-Plesset* equation,

$$\frac{p_{V(T_\infty)} - p_{(\mathbf{x},t)}}{\rho_L} + \frac{p_{Go}}{\rho_L}\left(\frac{R_o}{R}\right)^3 = R\frac{D^2R}{Dt} + \frac{3}{2}\left(\frac{DR}{Dt}\right)^2 + \frac{4\nu_L}{R}\frac{DR}{Dt} + \frac{2S}{\rho_L R}; \frac{D}{Dt} = \frac{\partial}{\partial t} + \mathbf{v}\cdot\nabla \tag{6}$$

and the definition,

$$\beta = \frac{\overline{V}_g}{1+\overline{V}_g}; \quad \overline{V}_g = \eta \tfrac{4}{3}\pi R^3 \tag{7}$$

Consider now the dynamic terms in the *Rayleigh-Plesset* equation. Any bubble in the squeeze film lands is subjected to a pressure, p, composed of a constant value, $\overline{p}$, plus an oscillating component, $\tilde{p}$, of a fundamental frequency equal to the journal whirl frequency, ω. If the frequency $\omega << \omega_n$, the bubble natural frequency, the contribution of the inertia terms will be negligible and the bubble will behave as quasi-static, unless it is within an unstable region. The natural frequency of the bubble extracted from the linear form of equation (6) is given by:

$$\omega_n = \sqrt{\frac{1}{\rho_L R_{eq}^2}\left[3\left(\overline{p}_\infty - p_V\right) + \frac{4S}{R_{eq}}\right]} \tag{8}$$

where the equilibrium bubble radius corresponds to a bubble at the mean pressure value, $\overline{p}$. For a typical test case (as discussed in the previous chapter), the mean pressure corresponds to the exit plenum pressure (~2.1×10^5 Pa), where visual observation of the bubbles suggests bubble radii similar to the damper clearance (R_{eq}~0.3 mm). The surface tension coefficient, S, of the ISO VG68 oil employed in the tests is equal to 0.035 N/m at the test temperature (T_∞=38 °C), the vapor pressure, p_V, is 0.08 Pa at the same temperature, and the oil density, ρ_L, is 867 kg/m^3.

Substitution of these values into equation (8) results in a natural frequency estimate of ω_n=14,300 Hz[4], which is much larger than the typical operating frequency of most *SFDs, i.e.* usually below 500 Hz. Furthermore, it seems more adequate to employ the liquid density for the inertial terms in the *RPE*. Yet, it is noted that consideration of the reduction of the effective mixture density due to the presence of the bubbles would lead to the prediction of even higher bubble natural frequencies. Recall, however, that even when the excitation frequencies are small with respect to the linearized bubble natural frequency for the mean bubble radius, the nonlinearities of the *RPE* could lead to conditions in which the dynamic terms are not negligible. Consequently, considering the bubbles as in quasi-static motion leads to a simplification of the *Rayleigh-Plesset* equation (6) to:

$$p_{V(T_\infty)} - p_{(\mathbf{x},t)} + p_{Go}\left(\frac{R_o}{R}\right)^3 = \frac{2S}{R} \tag{9}$$

Equation (9) provides a direct relation between the mixture pressure and the bubble radius. If the mixture pressure is known, the bubble radius can be directly computed and set into equation (7) to compute the gas volume fraction. Then, the effective density of the mixture can be estimated, providing closure to the continuity and momentum equations, (4) and (5), respectively, if the mixture viscosity is known. Further analysis of the terms in equation (9) leads to additional simplifications. While all the pressure terms on the left hand side are on the order of 10^5 Pa (1 bar), a typical value of the surface tension term on the right hand side is estimated as just 233,33 Pa (S=0.035 N/m, R=0.3 mm). Thus, the right hand side term is three orders of magnitude smaller than those in the left hand side and can be safely neglected. The *Rayleigh-Plesset* equation (9) can now be written in terms of the partial pressure of the gas, p_g, instead of the bubble radius as:

$$p_{V(T_\infty)} + p_g = p_{(\mathbf{x},t)} \tag{10}$$

which simply states that for a quasi-static bubbly mixture in the absence of surface tension the liquid pressure is in balance with the sum of the partial pressures of the vapor and the gas

[4] Note that the equation for the bubble natural frequency is based on the assumption of an infinite incompressible fluid medium surrounding the bubble.

contained within the bubbles. Thus, solving equation (10) for p_g and substituting into equation (7) leads to the following barotropic formulae for the mixture volume fraction:

$$\beta = \frac{1}{1 + \dfrac{p_{(x,t)} - p_V}{p_{Go}}\left(\dfrac{1}{\beta_o} - 1\right)} \tag{11}$$

Recapitulating, the motion of a quasi-static, isothermal, homogeneous bubbly mixture composed of an ideal gas (air) and a Newtonian incompressible liquid (oil) is fully determined by equations (5), (9) and (11). It is certainly acknowledged that this set of equations could be obtained in a shorter and apparently simpler way. However, the long path hereby followed to derive the mixture equations evidences all the simplifications introduced and gives insight into their effects on the expected results. It is also intended to provide a sound framework for more complex formulations to come in the future.

It remains to adjust the mixture model to the geometry of typical squeeze film flows. Descriptions of the classical lubrication theory for single component fluids are available in lubrication textbooks and even some fluid mechanics texts (Szeri, 1980, Childs, 1993, Schlichting, 1955). The characteristic film thickness, C, is much smaller than any other dimension scale in the film, thus leading to a formulation where curvature effects are not important. Furthermore, fluid inertia terms and non-cross film velocity gradients are negligible.

Consider a cylindrical *SFD* executing circular centered orbits (*CCOs*) as depicted in Figure 11. The journal does not spin, but it whirls at a frequency (ω) describing a circular orbit of radius (e) around the center of the housing. The attitude angle (ϕ) defines the direction of the line of centers (connecting the center of the journal with the center of the housing). For circular centered orbits, $\phi = \omega t$ and (θ) represents an angular coordinate relative to a frame that rotates synchronously with the shaft whirling motion (attached to the line of centers). The relative coordinate system (θ) is related to the absolute angular coordinate (Θ) by

$$\theta = \Theta - \omega t \tag{12}$$

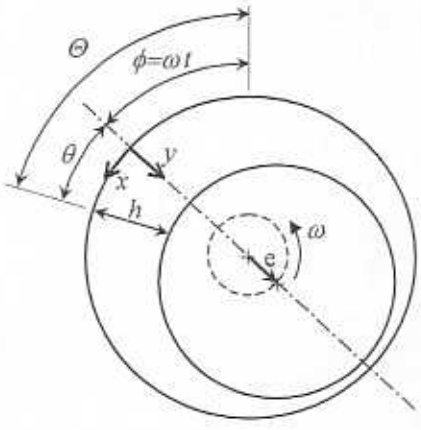

Fig. 11 Cylindrical squeeze film damper geometry.

The film thickness is given by:

$$h = C + e\cos(\theta) \tag{13}$$

The smallness of the film thickness (or radial clearance, C) allows the flow to be described with a local (unwrapped) Cartesian coordinate system as depicted in Figure 12. The y coordinate lies across the film, z is aligned with the shaft axis, and x represents the circumferential direction with

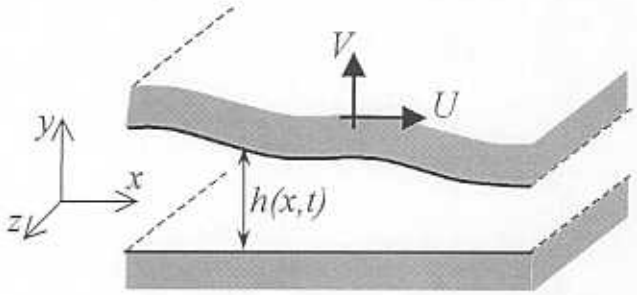

Fig. 12 Unwrapped *SFD* film land.

$$x = \frac{D}{2}\Theta \tag{14}$$

In the $\{x,y,z\}$ coordinate system of Figure 12, equations (4) and (5) become

Continuity:
$$\frac{\partial \rho}{\partial t} + \frac{\partial \rho v_x}{\partial x} + \frac{\partial \rho v_y}{\partial y} + \frac{\partial \rho v_z}{\partial z} = 0 \tag{15}$$

Momentum in x:
$$0 = -\frac{\partial p}{\partial x} + \frac{\partial}{\partial x}\left(\mu\frac{\partial v_x}{\partial x}\right) + \frac{\partial}{\partial y}\left(\mu\frac{\partial v_x}{\partial y}\right) + \frac{\partial}{\partial z}\left(\mu\frac{\partial v_x}{\partial z}\right) \tag{16}$$

Momentum in y:
$$0 = -\frac{\partial p}{\partial y} + \frac{\partial}{\partial x}\left(\mu\frac{\partial v_y}{\partial x}\right) + \frac{\partial}{\partial y}\left(\mu\frac{\partial v_y}{\partial y}\right) + \frac{\partial}{\partial z}\left(\mu\frac{\partial v_y}{\partial z}\right) \tag{17}$$

Momentum in z:
$$0 = -\frac{\partial p}{\partial z} + \frac{\partial}{\partial x}\left(\mu\frac{\partial v_z}{\partial x}\right) + \frac{\partial}{\partial y}\left(\mu\frac{\partial v_z}{\partial y}\right) + \frac{\partial}{\partial z}\left(\mu\frac{\partial v_z}{\partial z}\right) \tag{18}$$

Many correlations have been proposed for the effective viscosity of homogeneous bubbly mixtures, some of them contradicting each other. Feng and Hahn (1986), Pinkus (1990) and Camniprasart et al. (1993) present a compilation of the most used correlations for the mixture viscosity, namely:

Owens:
$$\mu = \mu_L \tag{19}$$

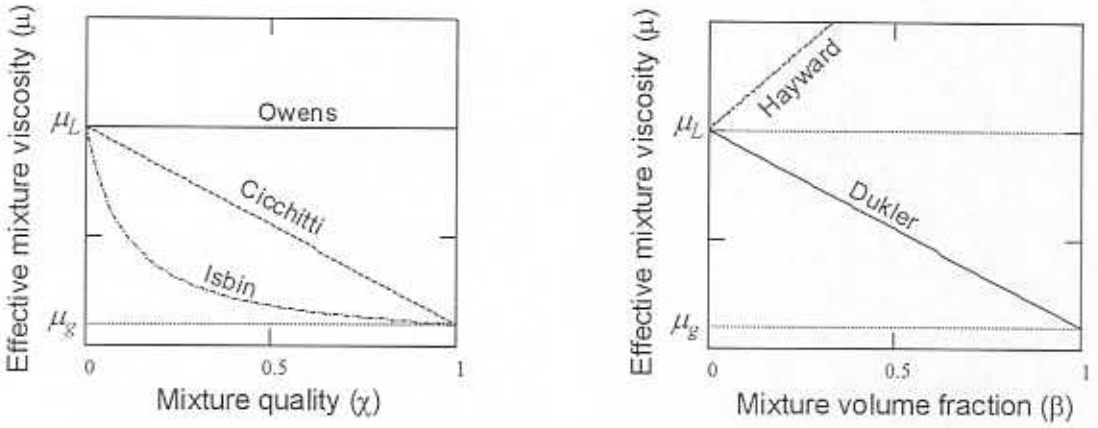

Fig. 13 Different correlations for the effective mixture viscosity.

Isbin: $$\mu = \frac{1}{\frac{\chi}{\mu_g} + \frac{(1-\chi)}{\mu_L}} \tag{20}$$

Cicchitti: $$\mu = \chi\,\mu_g + (1-\chi)\mu_L \tag{21}$$

Dukler: $$\mu = \chi\,\mu_g \frac{\rho}{\rho_g} + (1-\chi)\mu_L \frac{\rho}{\rho_L} \tag{22}$$

Hayward: $$\mu = \mu_L(1+1.5\beta), \quad \beta < 0.03 \tag{23}$$

where χ, represents the mass fraction (quality) of the gaseous component.

Owens approximation, eqn. (19), is evidently valid only for small gas volume fractions. Hayward's equation, (23) limited to small gas volume fractions comes from experimental measurements performed by Hayward (1961), and it is also based on Taylor's (1932) approximation of a theoretical formula developed by Einstein (1906) to estimate the viscosity of a fluid with a suspension of spherical particles.

The Isbin, Cicchitti, and Dukler relations predict an effective viscosity that varies smoothly from the value of the liquid viscosity to that of the gas as the mass fraction of gas increases. However, Isbin and Cicchitti predict constant mixture viscosity values for any homogeneous mixture, regardless of the volume fraction, because the mass fraction remains constant. On the other hand, as Dukler's relation introduces the phase densities, this equation does predict a smooth change of the viscosity as the volume fraction changes. As a matter of fact, Dukler's correlation can be rearranged to evidence the dependence of the viscosity on the volume fraction as follows

$$\mu = \beta\,\mu_g + (1-\beta)\mu_L \tag{24}$$

Figure 13 shows the different viscosity correlations versus the mixture quality or mixture volume fraction, depending on the case. Note that mixture qualities of zero and one correspond to volume fractions of zero and one, respectively. However, any mixture quality between the two extremes could correspond to any mixture volume fraction in the same range and vice versa.

For the air-oil mixture of interest, the viscosity of the liquid is several orders of magnitude larger than the viscosity of the gas. Thus, an approximation of the mixture viscosity can be obtained when the gas viscosity is neglected,

$$\mu = (1-\beta)\mu_L \tag{25}$$

This viscosity correlation, the only one that relates the viscosity to the component volume fractions for the whole range of compositions, is selected for estimation of the effective viscosity of the mixture.

Consider now the scale factors D (journal diameter), C (radial clearance) and L (damper axial length), in the x, y and z directions, respectively, and a characteristic frequency ω. Non-dimensional parameters can be defined as:

$$\begin{aligned} x &= D\,\hat{x} & v_x &= \omega D\,\hat{v}_x \\ y &= C\,\hat{y} & v_y &= \omega C\,\hat{v}_y \qquad t = \frac{\hat{t}}{\omega} \\ z &= L\,\hat{z} & v_z &= \omega L\,\hat{v}_z \end{aligned} \tag{26}$$

which, when introduced in the flow equations, render:

Continuity:
$$\frac{\partial \rho}{\partial \hat{t}} + \frac{\partial \rho \hat{v}_x}{\partial \hat{x}} + \frac{\partial \rho \hat{v}_y}{\partial \hat{y}} + \frac{\partial \rho \hat{v}_z}{\partial \hat{z}} = 0 \tag{27}$$

Momentum in x:
$$0 = -\frac{1}{D}\frac{\partial p}{\partial \hat{x}} + \frac{\omega}{D}\frac{\partial}{\partial \hat{x}}\left(\mu\frac{\partial \hat{v}_x}{\partial \hat{x}}\right) + \frac{\omega D}{C^2}\frac{\partial}{\partial \hat{y}}\left(\mu\frac{\partial \hat{v}_x}{\partial \hat{y}}\right) + \frac{\omega D}{L^2}\frac{\partial}{\partial \hat{z}}\left(\mu\frac{\partial \hat{v}_x}{\partial \hat{z}}\right) \tag{28}$$

Momentum in y:
$$0 = -\frac{1}{C}\frac{\partial p}{\partial \hat{y}} + \frac{\omega C}{D^2}\frac{\partial}{\partial \hat{x}}\left(\mu\frac{\partial \hat{v}_y}{\partial \hat{x}}\right) + \frac{\omega}{C}\frac{\partial}{\partial \hat{y}}\left(\mu\frac{\partial \hat{v}_y}{\partial \hat{y}}\right) + \frac{\omega C}{L^2}\frac{\partial}{\partial \hat{z}}\left(\mu\frac{\partial \hat{v}_y}{\partial \hat{z}}\right) \tag{29}$$

Momentum in z:
$$0 = -\frac{1}{L}\frac{\partial p}{\partial \hat{z}} + \frac{\omega L}{D^2}\frac{\partial}{\partial \hat{x}}\left(\mu\frac{\partial \hat{v}_z}{\partial \hat{x}}\right) + \frac{\omega L}{C^2}\frac{\partial}{\partial \hat{y}}\left(\mu\frac{\partial \hat{v}_z}{\partial \hat{y}}\right) + \frac{\omega}{L}\frac{\partial}{\partial \hat{z}}\left(\mu\frac{\partial \hat{v}_z}{\partial \hat{z}}\right) \tag{30}$$

Notice that the scale (C) in the cross film (y) direction is much smaller than any other, while D and L might be of the same order of magnitude. Typical C/D (or C/L) ratios are in the order of 1/500. Hence, the terms with the lower order in (C) dominate in equations (28) to (30). All the higher order terms on (C) are neglected, and the momentum equations simplify to

Momentum in x:
$$\frac{\partial p}{\partial \hat{x}} = \frac{\omega D^2}{C^2}\frac{\partial}{\partial \hat{y}}\left(\mu\frac{\partial \hat{v}_x}{\partial \hat{y}}\right) \tag{31}$$

Momentum in y: $$\frac{\partial p}{\partial \hat{y}} = 0 \tag{32}$$

Momentum in z: $$\frac{\partial p}{\partial \hat{z}} = \frac{\omega L^2}{C^2}\frac{\partial}{\partial \hat{y}}\left(\mu \frac{\partial \hat{v}_z}{\partial \hat{y}}\right) \tag{33}$$

Equation (32) states that the pressure is constant across the film thickness, a direct consequence of the smallness of the film clearance. Consequently, neither the density nor the viscosity of the mixture vary along the film thickness. This observation allows direct integration of the remaining momentum equations across the film,

$$\hat{v}_x = \frac{1}{2\mu\omega D^2}\frac{\partial p}{\partial \hat{x}}\left(C^2\hat{y}^2 - hC\hat{y}\right) \tag{34}$$

$$\hat{v}_z = \frac{1}{2\mu\omega L^2}\frac{\partial p}{\partial \hat{z}}\left(C^2\hat{y}^2 - hC\hat{y}\right) \tag{35}$$

where the following boundary (no slip) conditions have been enforced,

$$\begin{cases} at \;\; y = 0 \;\Rightarrow\; v_x = 0, \quad v_y = 0, \quad v_z = 0 \\ at \;\; y = h \;\Rightarrow\; v_x = U = 0, \quad v_y = V = \frac{dh}{dt}, \quad v_z = 0 \end{cases} \tag{36}$$

Note that the velocity components in the x and z directions are defined by a pressure gradient (Poiseuille flow).

The flow velocities just derived are inserted into the continuity equation (27). An integral form of this equation across the film lead to the well known Reynolds lubrication equation,

$$\omega\frac{\partial}{\partial \hat{t}}(\rho h) - \frac{1}{D}\frac{\partial}{\partial \hat{x}}\left[\frac{\rho h^3}{12\mu D}\frac{\partial P}{\partial \hat{x}}\right] - \frac{1}{L}\frac{\partial}{\partial \hat{z}}\left[\frac{\rho h^3}{12\mu L}\frac{\partial P}{\partial \hat{z}}\right] = 0 \tag{37}$$

Rewriting equation (37) by introducing the geometric relation (14), the Reynolds Equation becomes:

$$\overbrace{\omega\frac{\partial(\rho h)}{\partial \hat{t}}}^{(1)} - \overbrace{\frac{4}{D^2}\frac{\partial}{\partial \Theta}\left[\frac{\rho h^3}{12\mu}\frac{\partial P}{\partial \Theta}\right]}^{(2)} - \overbrace{\frac{1}{L^2}\frac{\partial}{\partial \hat{z}}\left[\frac{\rho h^3}{12\mu}\frac{\partial P}{\partial \hat{z}}\right]}^{(3)} = 0 \tag{38}$$

Analysis of the dimensions L and D renders two common simplifications to the general Reynolds equation for lubrication, the *infinitely long* and the *infinitely short* length bearing models. The long bearing model considers $L>>D$ and accordingly neglects the third term of the Reynolds equation (38), rendering a pressure field independent of the axial coordinate z. The short length bearing model considers $L<<D$ and drops the second term in the Reynolds equation. The infinitely long bearing model predicts well the pressure field in *SFDs* with sealed ends or with large L/D ratios, where the axial flow is negligible in comparison to the circumferential flow. The infinitely short length bearing has proven useful for the prediction of

pressure in open ends bearings with L/D ratios smaller than 0.5, where the axial flow is dominant. The L/D ratio of the SFD employed in the experimental measurements is equal to 0.24, thus the short length bearing model will be adopted hereafter for simplicity, i.e.

$$\omega \frac{\partial(\rho h)}{\partial \hat{t}} - \frac{1}{L^2}\frac{\partial}{\partial \hat{z}}\left[\frac{\rho h^3}{12\mu}\frac{\partial P}{\partial \hat{z}}\right] = 0 \tag{39}$$

Note that the short length bearing model, unlike the long bearing model does predict pressure gradients on the x and z directions. Thus equation (39) must be solved in a 2-dimensional domain.

The kinematic relation (12) allows rewriting the Reynolds equation in terms of the moving coordinate (θ), where the pressure profile appears stationary in time. Thus, the Reynolds equation for a short lentgh *SFD* performing *CCO*s and operating with a quasi-static, isothermal, homogeneous bubbly mixture is written as:

$$-\omega \frac{\partial}{\partial \theta}\left[\rho\left(C + e\,\cos(\theta)\right)\right] - \frac{1}{L^2}\frac{\partial}{\partial \hat{z}}\left[\frac{\rho\left[C + e\,\cos(\theta)\right]^3}{12\mu}\frac{\partial P}{\partial \hat{z}}\right] = 0 \tag{40}$$

where the effective mixture density, ρ, is given by the relation

$$\rho = (1-\beta)\rho_L, \tag{41}$$

$$\beta = \frac{1}{1 + \dfrac{p_{(x,t)} - p_V}{p_{Go}}\left(\dfrac{1}{\beta_o} - 1\right)}, \tag{11}$$

and the effective mixture viscosity, μ, is estimated with the Dukler's model

$$\mu = (1-\beta)\mu_L \tag{25}$$

Note that the dependence on the bubble radius has been removed from the simplified *Rayleigh-Plesset* equation. Therefore, the reference state is fully defined by the volume fraction at a certain known pressure. There is no need to estimate the size of the bubbles or the number of bubbles per unit volume of liquid. This certainly represents an advantage since the bubble size and concentration are difficult to measure with accuracy.

The solution of the Reynolds differential equation requires the definition of boundary conditions. These boundary conditions depend on the particular geometry studied. In general, the boundary conditions surrounding the flow domain correspond to:

(a) periodicity in the circumferential direction,
(b) known pressure at and open end,
(c) zero flow at a tightly sealed end or at a symmetry plane, or
(d) a relation between pressure and flow rate for a partially sealed (not tightly sealed) end (in this case the short length bearing model is no longer valid).

3.2 Predicted Forced Response of a *SFD* Operating with a Bubbly Mixture

The theoretical model developed is employed to estimate hydrodynamic pressures for the test *SFD* and the experiments conducted with controlled air-in-oil lubricant mixtures, depicted in Figure 2. The journal, of length L=31.1 mm and diameter D=129.4 mm, whirls describing circular orbits about the center of the housing. The radial clearance (gap) between the journal and the housing is C=0.343 mm. As previously discussed, the orbit radius measured in the experiments presents minute variations both in time and with the mixture volume fraction. However, rather than using the measured (different) orbit radius on each case, an average orbit radius (e=0.18 mm) is employed for the numerical calculations so that only the effects of the varying mixture composition are apparent in the results. For the same reason, the discharge plenum pressure is also set to the average value from the experimental measurements (P_o=1.8 bar). The reference state is taken as the pressure and mixture volume fraction at the exit plenum. These are available directly from the measurements.

A standard central differences scheme is devised for integration of the differential equation (67) and applying, as boundary conditions, periodicity in the circumferential direction, zero axial flow at the sealed end and a constant pressure value at the open end, i.e.,

$$\begin{cases} P_{(0,z)} = P_{(2\pi,z)} \\ P_{(L)} = P_o \\ \left.\frac{\partial P}{\partial z}\right|_{z=0} = 0 \end{cases} \tag{42}$$

For a given reference state (P_o,β_o), an initial pressure profile is taken as a constant value and equal to the plenum pressure ($P_{(\theta,z)}$=P_o). Then, equations (41) and (10) are used to compute the corresponding density field ($\rho_{(\theta,z)}$) and equation (25) to calculate the corresponding viscosity field ($\mu_{(\theta,z)}$). With this density and viscosity profiles, an improved pressure field is computed by solving the differential equation (40). Next, a corrected pressure profile is computed with an under-relaxation factor (α=0.1) such that

$$P_{corr(\theta,z)} = (1-\alpha)P_{old(\theta,z)} + \alpha\, P_{new(\theta,z)} \tag{43}$$

The corrected pressure field is employed to compute improved density and viscosity profiles, which in turn are used to compute film pressures in the iterative process. Converge criteria is based on a maximum difference of 2% between the old and new pressures

Note that for the numerical implementation, equation (11) is rewritten as:

$$\beta = \frac{\beta_o}{\beta_o + \dfrac{p_{(\mathbf{x},t)} - p_V}{p_{Go}}\left(1-\beta_o\right)}, \tag{44}$$

to eliminate the singularity at β_o=0 (i.e., pure liquid lubricant). Note that the difference $\left\{p_{(\mathbf{x},t)} - p_V\right\}$ equals the pressure of the non-condensable gas within the bubble, which shall be greater than zero at all times. However, since an iterative method is employed, it is possible for

the corrected pressure to take zero or negative values at some step during the calculations. Therefore, an additional condition is implemented which sets to a minimum value of 1 Pa any computed pressure below this value. This condition does not affect the final result for the practical cases in which an air-oil mixture is employed, since the absolute pressures are always above this value. Yet, for $\beta=0$ it allows the integration scheme to include the short length bearing model with lubricant vapor cavitation (i.e., for the pure oil condition all negative pressures are discarded).

Figure 14 depicts the computed circumferential pressure profiles for a whirl frequency of 8.33 Hz at the axial locations Z_1 and Z_2. The vertical axis represents the absolute film pressure and the horizontal axis corresponds to the angular location measured in the negative direction of the rotating reference frame. This representation is more appropriate for comparison with the experimental results since it corresponds to what a fixed observer would record during one period of journal motion. The horizontal axis depicts the time multiplied by the whirl frequency. The pressures are computed at equally spaced values of the reference mixture volume fraction (β_o=0, 0.1,...,1).

The hydrodynamic pressures computed for a pure oil condition are verified to replicate the analytical solution of equations (1) and (2). The solution for pure oil predicts vapor cavitation at the axial location Z_2. However, recall that according to the model employed for the pure oil condition the pressure generation outside of the vapor cavitation zone is identical to that of an uncavitated film (i.e., the effect of the occurrence of vapor cavitation on the pressures outside the cavitation zone is neglected). This fact might justify the large difference on the pressure fields when the volume fraction is increased from 0 to 0.1. Yet, it is also clear from the experimental results of Diaz and San Andrés (1997, 1998 a-c) that precisely in this range of volume fractions the pressures are more sensitive to changes in the mixture composition than in any other.

As in the experimental results, the pressure at the maximum film thickness ($\theta = 0$) is equal to the side pressure regardless of the mixture composition. In all cases the positive hydrodynamic pressure peak is larger than the minimum, and as the mixture volume fraction increases, the location of the maximum peak moves towards the location of minimum film thickness.

The uniform pressure zone observed in the experimental pressure profiles is not readily apparent from the predicted pressure profiles. Figure 15 provides a waterfall-like representation of the pressure profiles similar to that used in the experimental cases of Diaz and San Andrés (1997, 1998a-c). The vertical axis represents the squeeze film pressure, the horizontal axis depicts the time multiplied by the whirl frequency, and the in-plane axis denotes the mixture volume fraction. The computed results of Figure 15a correspond to the axial location Z_1, and those in Figure 15b to the axial location Z_2, both predicted at a whirl frequency of 8.33 Hz. The extent of the zone of uniform pressure is depicted, showing that even though the pressure is not constant, the pressure changes are small within that zone. Figure 16 reproduces the results of Figure 15 as 3D surfaces. The uniform pressure zone is depicted, increasing its extents as the mixture volume fraction increases and with a pressure independent of the mixture composition.

Figure 17 shows contour plots of the above-described 3D pressure surfaces on the time-mixture volume fraction plane along with the local film thickness depicted on the same time scale. This representation allows the correlation of the pressure fields with the local film thickness and the mixture volume fraction at the same time. Positive hydrodynamic pressures are generated during the positive squeeze portion of the cycle (decreasing film thickness). Negative hydrodynamic pressures occur during the negative squeeze (increasing film

thickness). The maximum pressure peak moves towards the point of minimum film thickness as the volume fraction increases from zero. Two lines denote the area corresponding to the uniform pressure zone of the experiments to lie on a zone of small pressure changes that develops around the zone of maximum film thickness and covering the last part of the negative squeeze motion and the first part of the positive squeeze. Further analysis is required to identify the mechanism that leads to the formation of the uniform pressure zone and to include this phenomenon in the theoretical models.

It is possible that a large air bubble develops interrupting the continuity of the *homogenous bubbly mixture* in the film, as in the case of vapor cavitation, and preventing the hydrodynamic pressure build up. Another possibility is that the dynamic terms of the *Rayleigh-Plesset* equation, neglected in this model, could lead to unstable growth of the bubbles when the pressure is small enough and thus affect the squeeze film pressure generation. An experimental investigation including film flow visualization is required to elucidate this important issue.

Figure 18 shows a comparison of the peak-to-peak amplitude of the predicted pressures with the measurements previously described. The continuous lines depict the computed peak-to-peak pressures, the dotted lines represent the experimental measurements. In Figure 18a the experimental values correspond directly to the measurements on the transducer located at 330°,

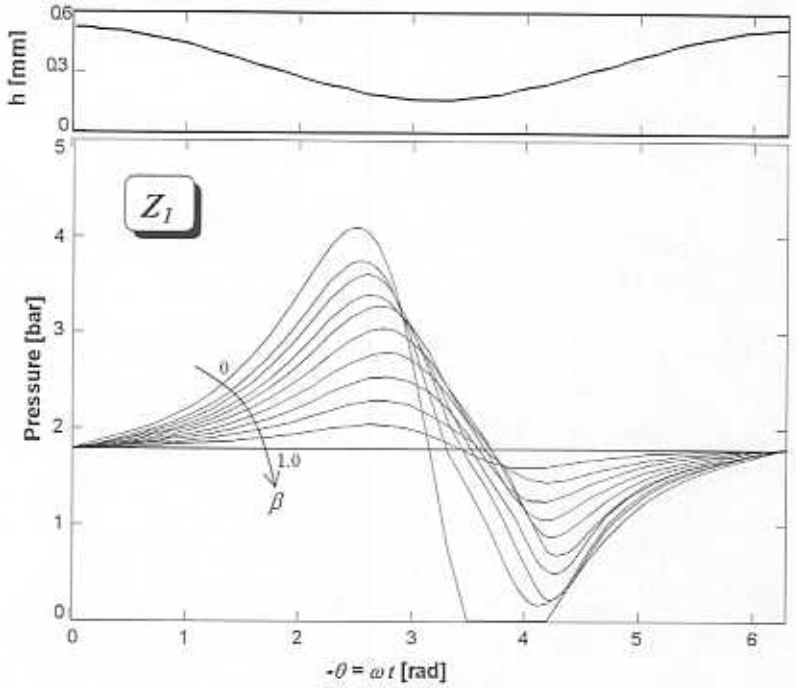

(a) axial location Z_1

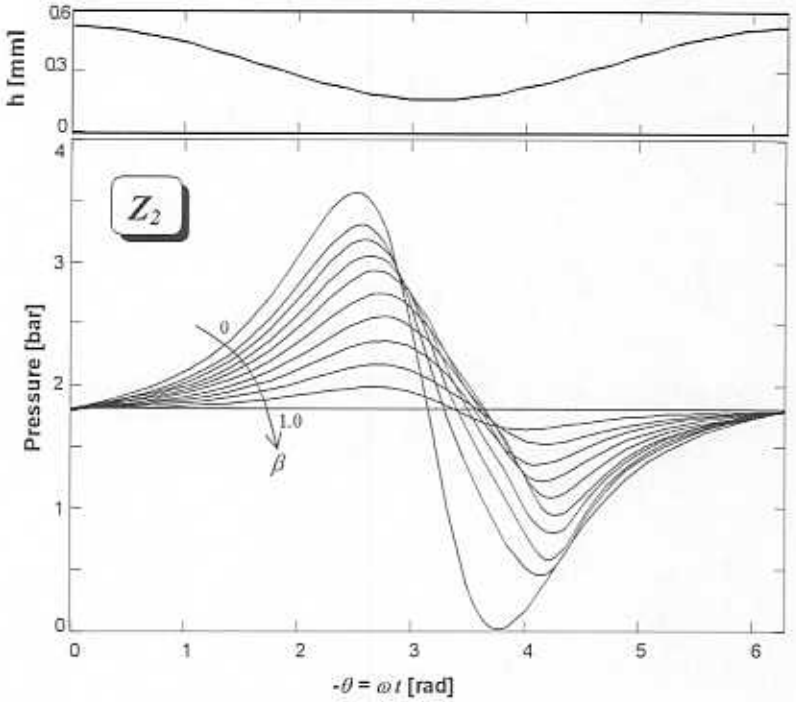

(b) axial location Z_2

Fig. 14 Predicted pressure profiles at a whirl frequency of 8.33 Hz for increasing mixture volume fraction at two different axial locations.

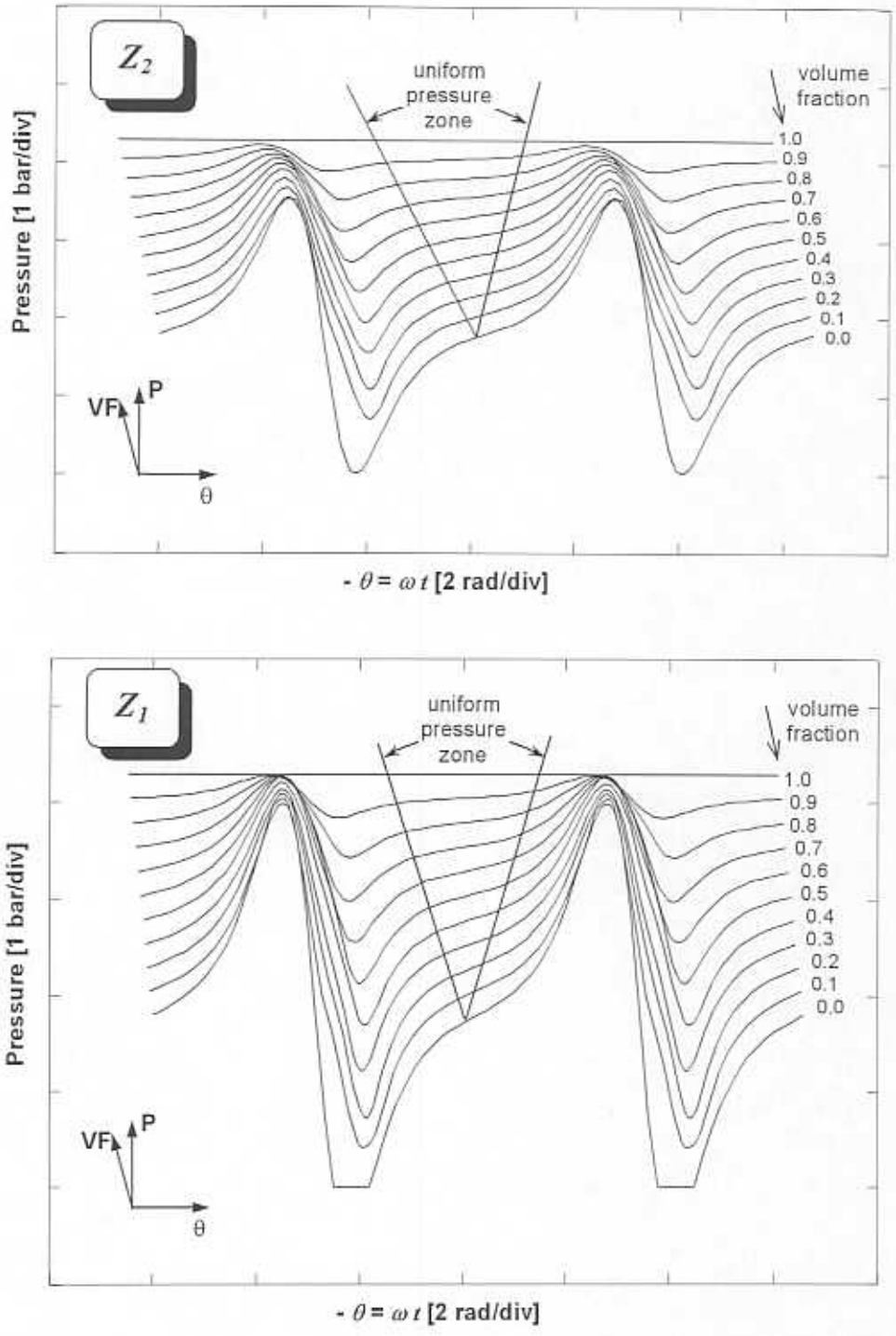

Fig. 15 Development of the predicted pressure fields with the mixture volume fraction for a whirl frequency of 8.33 Hz at two axial planes. (uniform pressure zone identified from test results).

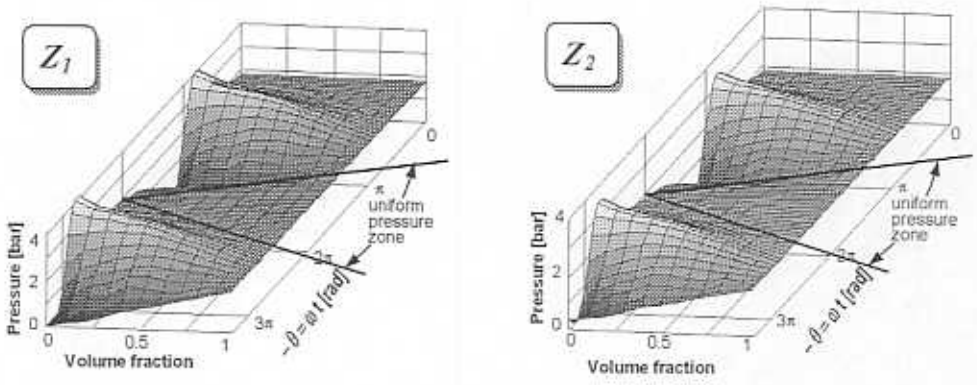

Fig. 16 3-D plots of the computed pressure fields versus the mixture volume fraction for a whirl frequency of 8.33 Hz at two different axial locations.

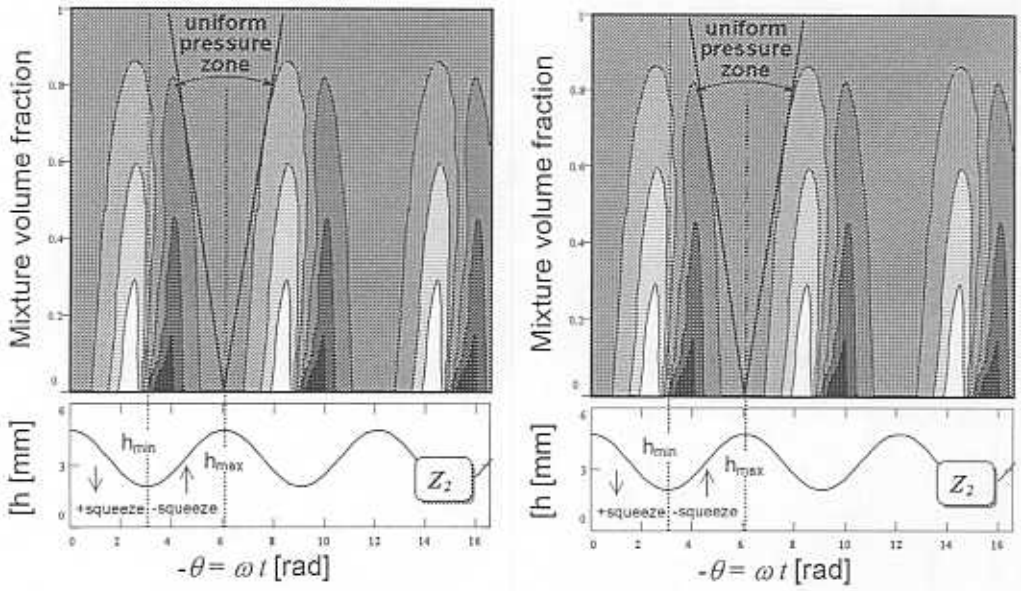

Fig. 17 Contour plots of the computed pressure fields versus the mixture volume fraction for a whirl frequency of 8.33 Hz at two different axial locations.

Z_1 (the only one available at this axial location). The vertical bars correspond to the first order uncertainty in those measurements.

In Figure 18b the experimental values correspond to the average of the measurements from all the transducers located at the axial plane of Z_2. In this case the vertical bars represent the variations both temporal and spatial by taking the maximum and minimum values ever, anywhere. The computed pressures present a fast drop in peak-to-peak amplitude for small increments of the mixture volume fraction from β_o=0. After the initial drop, the peak-to-peak

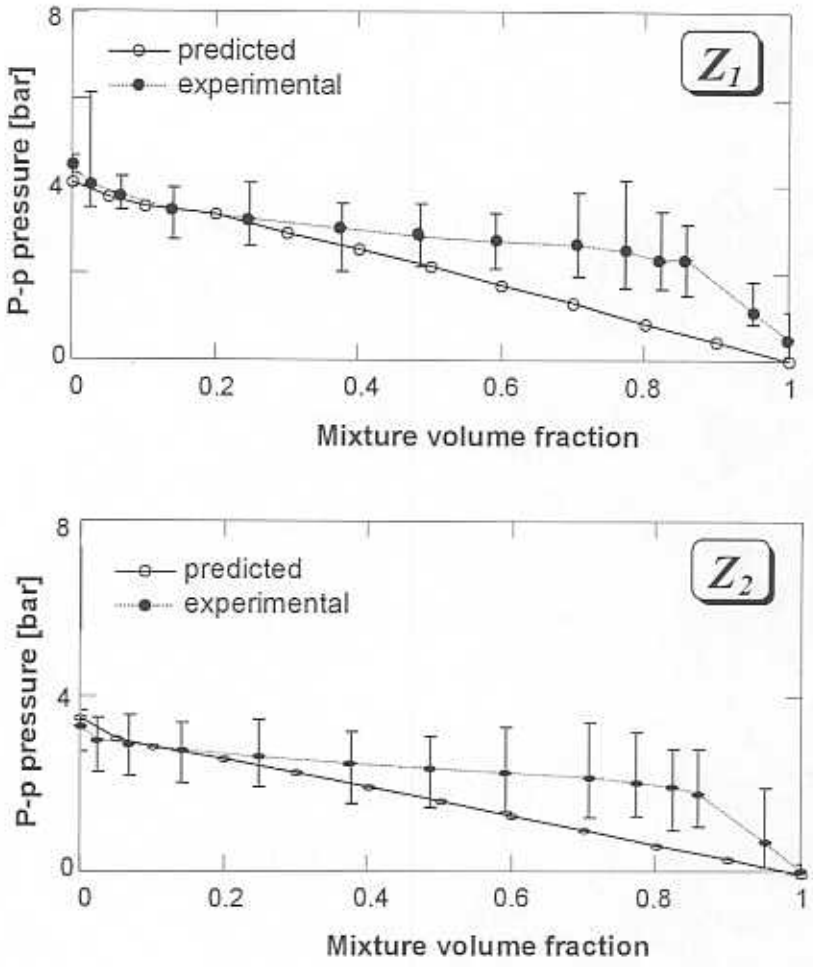

Fig. 18 Predicted and experimental peak-to-peak pressure amplitude for a whirl frequency of 8.33 Hz versus the mixture volume fraction at two different axial locations.

pressures decrease linearly with the mixture volume fraction to a null value when the volume fraction equals one. The peak-to-peak hydrodynamic pressure amplitudes are always larger at the axial location Z_1.

For low volume fractions the theoretical predictions present good agreement with the experimental measurements, but for mid to high concentrations of air the predictions diverge rapidly from the measurements. On the limit case of operation with pure air, both experimental and theoretical results render null values.

Figure 19 compiles the radial and tangential forces per unit length at the axial locations Z_1 and Z_2, for a whirl frequency of 8.33 Hz. The continuous lines represent the theoretical predictions, the dotted lines depict the experimental measurements. Squares and circles denote radial and tangential forces respectively. At the axial plane Z_2, the predicted radial force for the pure oil condition is null. However, at the plane Z_1 the model predicts a small radial component

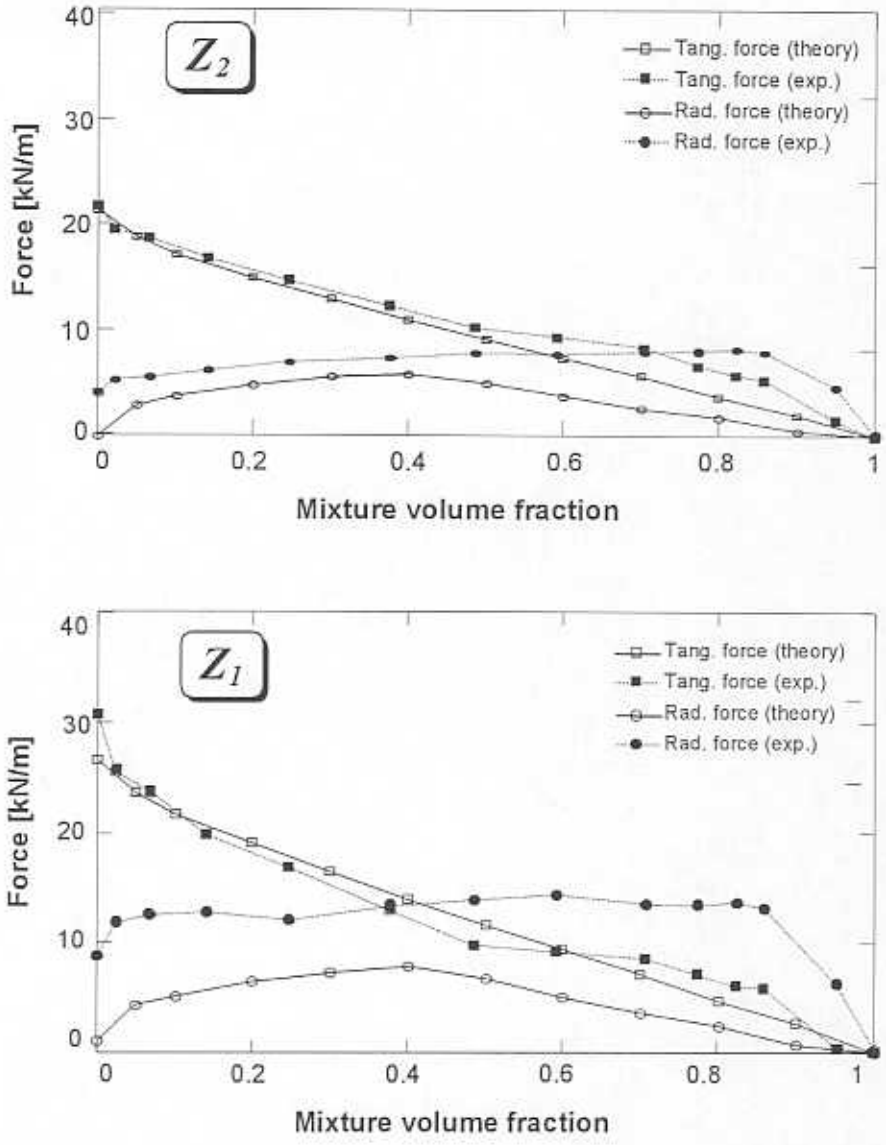

Fig. 19 Predicted and experimental hydrodynamic forces per unit length for a whirl frequency of 8.33 Hz at two different axial locations.

of the force due to the presence of vapor cavitation. None of the experimental measurements at either axial location shows null radial forces for pure oil lubricant operation. Nevertheless, recall that this component of the force has been related to a hydrostatic pressure drop due to the axial flow through the damper and the oil supply mechanism in the experimental rig, which is not considered in the present model.

For an incompressible lubricant the Reynolds equation is a linear operator, thus superposition of the hydrodynamic and hydrostatic pressure fields, as previously described in the

experimental results section, is possible. Consequently, superposition of the two pressure fields at β_o=0 (pure oil) can be assumed for the experimental and model predictions.

The hydrodynamic pressure and its associated forces can be estimated as the difference of the dynamic measurements minus the hydrostatic values. As a result, the measured hydrodynamic pressure profile and tangential force would remain virtually unchanged. Yet, the radial forces would become almost zero, as predicted by the model. Unfortunately, when the density and the viscosity are functions of the pressure, as it happens for volume fractions other than zero, the Reynolds equation is not a linear operator and superposition is no longer possible. It is suspected that the consideration of the axial flow would improve the agreement between predicted and measured radial forces, but this will imply modifications to the boundary conditions used in the model. However, note that the axial flow in the experiments was set to an unusually high value in order to assure a uniform lubricant mixture. In practical applications the contribution of the hydrostatic pressure field would be negligible.

The tangential force presents a similar behavior to that of the peak-to-peak pressures in both axial planes. It presents a sharp descent for small gas volume fractions and a linear relation to the volume fraction with a smaller reduction rate as it decreases to a null value at β_o=1. Theoretical predictions and experimental measurements present excellent agreement for low to medium values of mixture volume fractions. For volume fractions above 0.5, the measured forces deviate from a straight line and the theoretical predictions do not follow them well. Similar trends are observed for the forces and peak-to-peak-pressures for operation at 16.67 Hz (1,000 rpm).

Figure 20 shows the radial and tangential forces at the plane of Z_2. The bars, denoting the highest and lowest values obtained from integration of the pressures measured at different circumferential locations on the damper, give a measure of the variation in the forces due to the (lack of) journal centering, the deviation from an actual circle of the journal orbit, and/or the local conditions in the bubbly mixture.

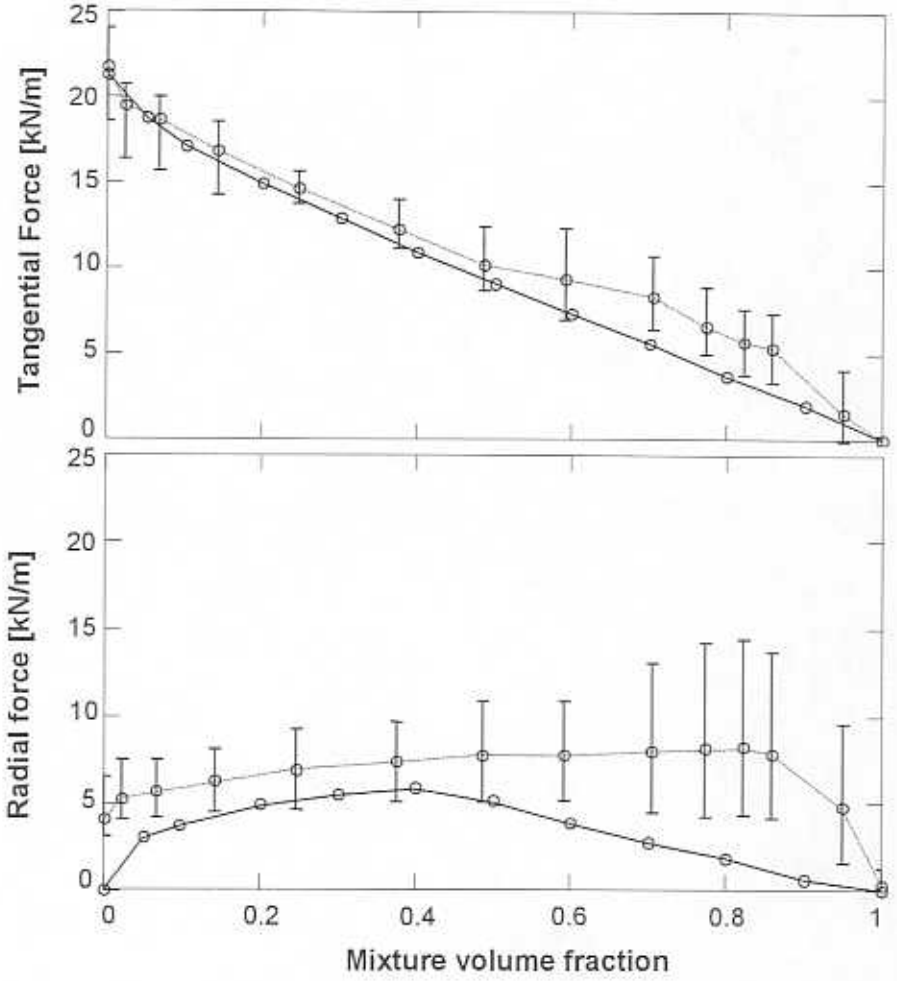

Fig. 20 Predicted and experimental hydrodynamic forces (radial and tangential) for a whirl frequency of 8.33 Hz at the axial location Z_2, including experimental uncertainty.

4. A MODEL FOR AIR ENTRAINMENT IN SQUEEZE FILM DAMPERS

4.1 Prediction of the Average Volume Fraction in an Open End Squeeze Film

Many factors affect the amount of air ingested into the squeeze film lands and trapped as a bubbly mixture with the lubricant. Among these factors are the supply and discharge pressures, the lubricant axial flow rate, the whirl frequency, the journal vibration amplitude, and the particular geometry of the damper. A quantification of the air/oil mixture composition is of interest for the accurate prediction of the dynamic performance of *SFDs*.

A simple analysis based on the balance of axial flows follows to compute the average air volume fraction of the lubricant mixture generated in a squeeze film damper operating with an end open to ambient conditions.

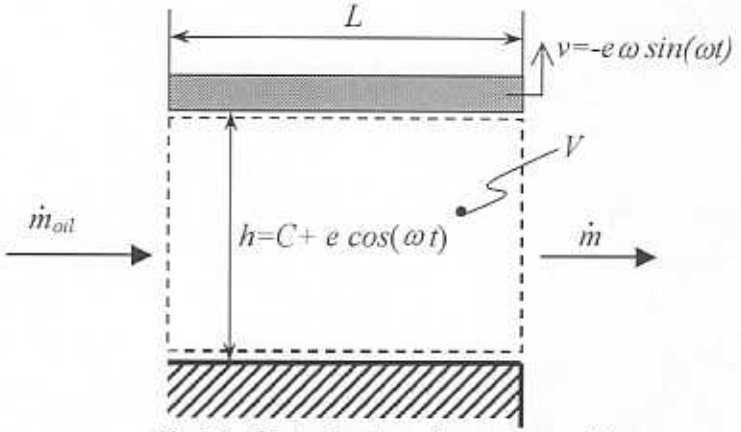

Fig. 21. Control volume in a squeeze film.

Consider the control volume shown in Figure 21. The top surface moves vertically with a harmonic velocity, $v=-e\,\omega\,sin(\omega t)$, squeezing the fluid contained within the control volume (per unit depth), $V = hL = L(C + e\,cos(\omega t))$. A constant oil in-flow rate, $\dot{m}_{oil}$, flows from the left end of the film, while the right side of the film is open to ambient, i.e., vented to an air or gaseous environment. The conservation of mass, per unit depth of film, over the control volume is

$$\dot{m}_{oil} - \dot{m} = \frac{\partial}{\partial t}(\rho_{mix} V) \tag{45}$$

The ambient discharge plenum is regarded both as a sink of oil and a source of air (gas) simultaneously. Any oil poured out of the end plane will be immediately drained away. Any flow entering from the ambient into the film will contain only air. Therefore, the flow through the end side, $\dot{m}$, is defined as:

$$\dot{m} = \begin{cases} -\dot{m}_{air} & if \quad \dot{m} < 0 \\ \dot{m}_{mix} & if \quad \dot{m} \geq 0 \end{cases} \tag{46}$$

where the instantaneous air flow $\left(\dot{m}_{air}\right)$ and mixture flow $\left(\dot{m}_{mix}\right)$ are defined as:

$$\dot{m}_{air} = \begin{cases} \rho_{air}\, q_{air} > 0 & if \;\; \dot{m} < 0 \\ 0 & if \;\; \dot{m} \geq 0 \end{cases} \quad ; \quad \dot{m}_{mix} = \begin{cases} 0 \; if \; \dot{m} < 0 \\ \rho_{mix_o}\, q_{mix} \geq 0 \; if \; \dot{m} \geq 0 \end{cases} \tag{47}$$

Assume that a periodic steady state condition has been reached. Thus, integrating equation (45) over one full period of motion of the moving top surface renders

$$\int_{t_o}^{t_o+\frac{2\pi}{\omega}} \rho_{oil} q_{oil} dt + \int_{t_o}^{t_o+\frac{2\pi}{\omega}} \rho_{air_o} q_{air} dt - \int_{t_o}^{t_o+\frac{2\pi}{\omega}} \rho_{mix_o} q_{mix} dt = \int_{t_o}^{t_o+\frac{2\pi}{\omega}} \frac{\partial}{\partial t}\left(\rho_{mix} V\right) dt \tag{48}$$

where $\dot{m}_{oil} = \rho_{oil}\, q_{oil}$.

At steady state[5], all flow variables have a fundamental period equal to that of the excitation frequency $(2\pi/\omega)$. Thus, the right hand side of equation (48) reduces to

$$\int_{t_o}^{t_o+\frac{2\pi}{\omega}} \frac{\partial}{\partial t}\left(\rho_{mix} V\right) dt = \left(\rho_{mix} V\right)\Big|_{t_o}^{t_o+\frac{2\pi}{\omega}} = 0 \tag{49}$$

i.e., the overall change in mass over a full period of motion equals zero.

Air enters the film at ambient conditions. Hence, the air density, ρ_{air_o}, in the second term of equation (48) is a constant and can be taken out of the integral. The oil density is also constant, because the pure lubricant is considered incompressible. The effective density of the mixture leaving the film is substituted by an average density, $\hat{\rho}_{mix_o}$. Equation (48) is then expressed as

$$\rho_{oil}\, \overline{q}_{oil} + \rho_{air_o}\, \overline{q}_{air} - \hat{\rho}_{mix_o}\, \overline{q}_{mix} = 0 \tag{50}$$

where

$$\overline{q}_{oil} = \frac{\omega}{2\pi} \int_{t_o}^{t_o+\frac{2\pi}{\omega}} q_{oil}\, dt = q_{oil}\,, \quad \overline{q}_{air} = \frac{\omega}{2\pi} \int_{t_o}^{t_o+\frac{2\pi}{\omega}} q_{air}\, dt\,, \text{ and } \overline{q}_{mix} = \frac{\omega}{2\pi} \int_{t_o}^{t_o+\frac{2\pi}{\omega}} q_{mix}\, dt$$ are the are

the average flow rates of oil supplied, of air entering, and of mixture leaving the film per unit depth, respectively. Note that the $\overline{q}_s$ correspond to flow rates averaged over a sufficiently long period of time which includes many fundamental periods of motion.

The mixture exits the film at ambient pressure and the entire process is regarded as isothermal. Thus, the air density in the discharge mixture is also equal to ρ_{air_o}. Therefore, by definition the average mixture density is

$$\hat{\rho}_{mix_o} = \hat{\beta}_o \rho_{air_o} + \left(1 - \hat{\beta}_o\right)\rho_{oil} \tag{51}$$

---

[5] Steady state here means after many periods of journal motion.

where $\hat{\beta}_o$ is the average volume fraction of the mixture leaving the film at ambient pressure, p_o. Applying conservation of mass independently for each component (air and oil) and integrating each equation over one period of motion, as performed earlier to obtain the continuity equation (50), yields the following two equations,

$$\begin{cases} \rho_{air_o}\overline{q}_{air} - \rho_{air_o}\hat{\beta}_o\,\overline{q}_{mix} = 0 \\ \rho_{oil}\,\overline{q}_{oil} - \rho_{oil}\left(1-\hat{\beta}_o\right)\overline{q}_{mix} = 0 \end{cases} \tag{52}$$

Solving the system of equations (52) for the mixture flow and its volume fraction gives

$$\overline{q}_{mix} = \overline{q}_{oil} + \overline{q}_{air} \tag{53}$$

$$\hat{\beta}_o = \frac{\overline{q}_{air}}{\overline{q}_{oil} + \overline{q}_{air}} \tag{54}$$

Equation (53) states that the mixture that exits the film during one period contains the same volume of air and oil that enters the film in one period. This is, of course, a consequence of having the same inlet and outlet pressures and temperatures, and thus, the same inlet and outlet densities for the compressible phase (air). In consequence, equation (54) provides not only the volume fraction of the mixture leaving the film, but also the proportion of the air and oil flows entering the film.

Consider now the portion of fluid within the control volume before a period of motion starts, and the one that remains in after a full period is completed. Since the flow is periodic, the fluid inherited from the preceding period has to be equivalent to that left for the succeeding one, i.e., it has to occupy the same volume and must have the same composition. Analytically, the "residing" fluid could be pure air, pure oil or a mixture of the two materials. However, the fluid transferred from one period to another does not necessarily have to contain the same material particles of the one inherited from the previous cycle. On the contrary, it is speculated that the fluid contained in the film mixes with the air and oil flows entering from different locations and, after a number of cycles, reaches a steady state composition. This equilibrium composition has to be necessarily equal to the composition of the mixture flowing through the film (recall that the mixture entering has the same composition than the one leaving).

As a result, the mixture leaving the film can be considered as representative of the whole mixture contained in the control volume and can be regarded as a reference state. Consequently, the mixture density becomes only a function of the local pressure, and the average density can then be approximated as the density at the average pressure. The experiments Diaz and San Andrés (1997, 1998 a-c) show that when operating with a bubbly mixture the average or mean pressure in the film is equal to the pressure at the open end boundary (p_o) (Diaz and San Andrés, 1997, 1998a-c). Thus, the average mixture density can be approximated as

$$\hat{\rho}_{mix} = \hat{\rho}_{mix_o} = \hat{\beta}_o\rho_{air_o} + \left(1-\hat{\beta}_o\right)\rho_{oil} \tag{55}$$

From equation (54), it only remains to determine $\overline{q}_{air}$ to fully define the reference state volume fraction. Integration of the continuity equations over the part of the period in which air

is being drawn into the film ($q_{air}>0$), and employing the average mixture density of equation (55), results in the following equations for the mass conservation of the air and oil components,

$$\begin{cases} \rho_{air_o} \int_{t_o}^{t_1} q_{air}\, dt = \hat{\beta}_o \rho_{air_o} \int_{t_o}^{t_1} \frac{\partial V}{\partial t} dt \\ \rho_{oil} \int_{t_o}^{t_1} q_{oil}\, dt = \left(1 - \hat{\beta}_o\right) \rho_{oil} \int_{t_o}^{t_1} \frac{\partial V}{\partial t} dt \end{cases} \tag{56}$$

where the interval $[t_o, t_1]$ corresponds to the time interval in which $q_{air}>0$. Canceling the densities and adding equations (56) renders

$$\int_{t_o}^{t_1} q_{air}\, dt = \int_{t_o}^{t_1} \left(\frac{\partial V}{\partial t} - q_{oil}\right) dt \tag{57}$$

or, evaluating the integrals,

$$\overline{q}_{air} = \frac{\omega}{2\pi}\left[\left(V_{(t_1)} - V_{(t_o)}\right) - q_{oil}\left(t_1 - t_o\right)\right] \tag{58}$$

In words, equation (58) states that when the film volume grows fast enough, $q_{air}>0$, the volume not filled by the lubricant is filled by air. In the interval $[t_o, t_1]$ the integrand of equation (57) is always positive

$$q_{air} = \frac{\partial V}{\partial t} - q_{oil} = Le\,\omega\ sin\left(\omega\, t\right) - q_{oil} > 0 \tag{59}$$

Thus, t_o and t_1 can be computed for the time values making equation (59) equal to zero (see Figure 22):

$$\begin{cases} t_o = -\frac{1}{\omega} sin^{-1}\left(\frac{q_{oil}}{Le\,\omega}\right) \\ t_1 = \frac{\pi}{\omega} - t_o \end{cases} \tag{60}$$

Substituting these values into equation (58) renders:

$$\overline{q}_{air} = \frac{\omega}{2\pi}\left[\frac{q_{oil}}{\omega}\left(2\ sin^{-1}\left(\frac{q_{oil}}{Le\,\omega}\right) - \pi\right) + 2Le\sqrt{1 - \left(\frac{q_{oil}}{Le\,\omega}\right)^2}\right] \tag{61}$$

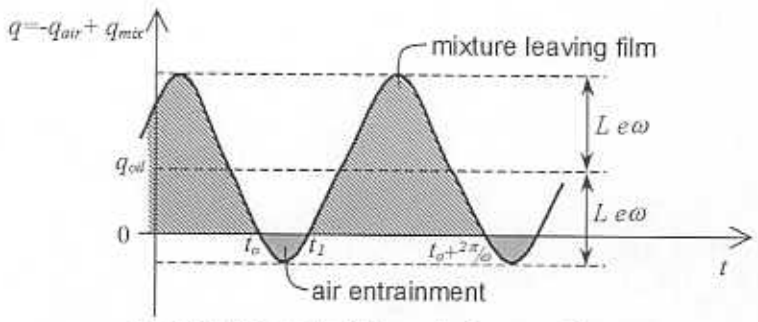

Fig. 22 Flow out of the end plane vs. time.

Finally, the average mixture volume fraction, or the reference state volume fraction, can be computed from equation (54) as

$$\hat{\beta}_o = \frac{\frac{q_{oil}}{\omega}\left(2\ sin^{-1}\left(\frac{q_{oil}}{Le\omega}\right)-\pi\right)+2Le\sqrt{1-\left(\frac{q_{oil}}{Le\omega}\right)^2}}{q_{oil}\frac{2\pi}{\omega}+\frac{q_{oil}}{\omega}\left(2\ sin^{-1}\left(\frac{q_{oil}}{Le\omega}\right)-\pi\right)+2Le\sqrt{1-\left(\frac{q_{oil}}{Le\omega}\right)^2}} \tag{62}$$

Define the dimensionless parameter, γ, as:

$$\gamma = \frac{q_{oil}}{Le\omega} \tag{63}$$

to represent the ratio of the supplied oil flow to the magnitude of the squeeze flow required to fill immediately any instantaneous (dynamic) variation of the film volume. As Figure 22 shows, air entrainment occurs only when (γ) is less than one and will increase as (γ) approaches zero. Combining equations (62) and (63) shows that the reference volume fraction is only a function of (γ), i.e.,

$$\hat{\beta}_{o(\gamma)} = \left(1+\frac{2\pi\gamma}{\gamma\left(2\ sin^{-1}(\gamma)-\pi\right)+2\sqrt{1-\gamma^2}}\right)^{-1} \tag{64}$$

Figure 23 shows the air volume fraction of the mixture trapped in the film, β_o, at the reference pressure, p_o, as a function of the dimensionless parameter (γ). The air volume fraction is equal to one for (γ) equal zero, i.e., in the steady state the control volume is filled only with air if oil is not continuously fed. As (γ) increases, i.e., the oil flow rate increases in relation to the dynamic volume change, the amount of air ingested into the film reduces and so does the air/oil volume fraction. When (γ) reaches one, the oil flow is just enough to completely fill the increasing volume and no air is drawn into the film. The air volume fraction is zero. For (γ) larger than one, the oil flow exceeds the required flow to fill the growing volume and the flow through the right end of the control volume (Figure 21) is always outwards, completely preventing air entrainment to the film. In the later case, the air volume fraction is equal to zero, and equation (64) is undefined.

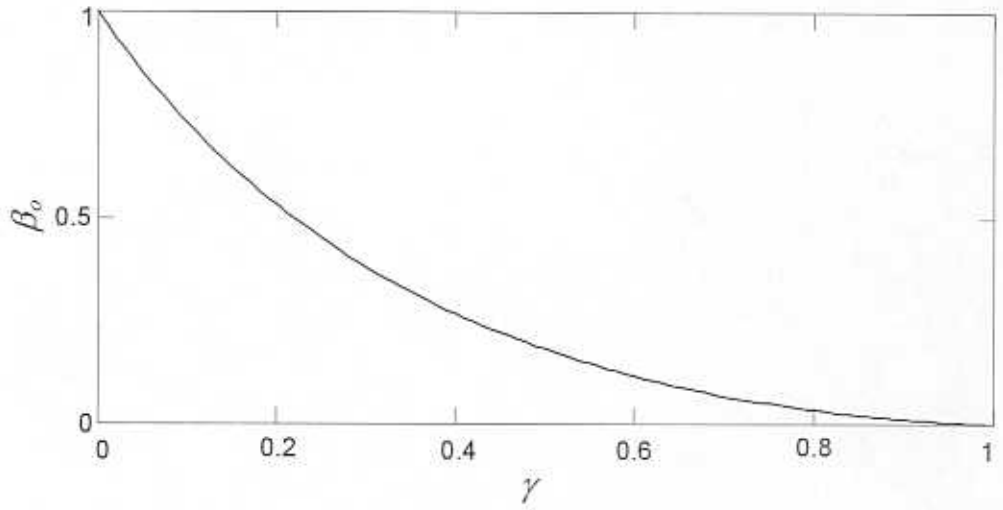

Fig. 23 Average air volume fraction vs. γ.

In the short length bearing model, the lubricant flow in the circumferential direction is negligible with respect to the flow in the axial direction. Thus, equation (64) is applicable to short length cylindrical *SFDs* executing circular orbits (*CCOs*), and where L corresponds to the axial length of the damper, e is the orbit radius, ω is the whirl frequency, and q_{oil} is the axial lubricant flow rate per unit arc length, i.e.

$$q_{oil} = \frac{Q_{oil}}{\pi D} \tag{65}$$

where D is the journal diameter and Q_{oil} is the total oil flow rate fed to the *SFD*. The equations are valid whether the *SFD* presents a configuration with an open end on one side and sealed on the other or with both sides open. In this last case both the journal length and the oil flow rate must be divided by two. Note that the one-half factors cancel each other in the definition of the (γ) parameter.

Applied to a cylindrical *SFD*, equation (45) represents a local balance of mass at a fixed circumferential location. The cylindrical symmetry of the *SFD* results in a stationary pressure field in a rotating coordinate system synchronous with the journal whirl motion. This allows the definition of a kinematic relation between the variation of the flow at a fixed location over one period and the variation of the flow along the damper circumference at a fixed time. Consequently, integration of the flows over time is equivalent to integration of the flows in the circumferential direction. Therefore, the flow rates in equation (50) not only refer to the total flow that enters or exits certain location of the film over one motion period but are also representative of the flows going in or out of the whole *SFD* at any instant in time. Thus, equation (64) renders the time average of the volume fraction at one location as well as the spatial average at any time. The (γ) parameter for *SFDs* executing *CCOs* is redefined as:

$$\gamma = \frac{Q_{oil}}{\pi D L e \omega} \tag{66}$$

Equations (64) and (66) explicitly show that the air volume fraction of the mixture trapped within the *SFD* lands depends on the supplied oil flow rate (Q_{oil}), the damper geometry (L, D), and the kinematics of the journal motion (e, ω).

Some other factors that affect the air entrainment are also implicit in this relationship. The oil flow rate is directly related to the supply and discharge pressures through the characteristic pressure losses in the supply and discharge devices as well as through the damper lands. Therefore, the (γ) number is also related to the damper clearance (C), supply and discharge pressures (P_s, P_o), oil viscosity (μ), and the oil supply configuration (injection holes, feeding grove, etc.) through the value of the oil flow (Q_{oil}). In summary, as noted in the literature, air entrainment is device dependent, increases with the amplitude and frequency of motion, and can be prevented by providing enough external pressurization to ensure a sufficiently large oil flow rate. This condition, of course, may not be readily available in practice.

4.2 Experimental Quantification of the Volume of Air Entrapped

Direct measurement of the amount of air entrapped in a *SFD*'s lubricant film due to free air entrainment is a virtually impossible task. Quantification of the volume of air entrapped in the film can only be attained by measurement of its effects on easily measured variables. Diaz and San Andres (1997, 1998a-c) describe in detail the effects of the introduction of controlled amounts of air in the lubricant on the hydrodynamic pressure generation and its associated forces in a *SFD*, thus evidencing the relation between the pressures and forces and the mixture volume fraction. Peak-to-peak pressure amplitudes and radial and tangential forces are presented versus the mixture volume fraction. Thus, the knowledge of the damper forces or the peak-to-peak pressures could help to determine the volume of air entrapped. However, this procedure requires knowledge of the particular squeeze film damper, operating at an identical speed and with the same orbit radius. This is certainly not an efficient procedure.

Recall that the experimental results demonstrate the occurrence of a zone of uniform or constant pressure that develops around the zone of maximum film thickness and whose extent is related to the amount of air in the lubricant mixture. This constant pressure zone is unique to the operation of *SFDs* with air in oil mixtures and has been observed for both operations with controlled bubbly mixtures as well as with air freely entrained.

An algorithm to measure the extent of this uniform pressure zone is applied to all the pressure profiles for the tests with controlled mixtures of air and oil. The algorithm sets a threshold band around the pressure corresponding to the time of maximum film thickness. Then the first pressure value that lies outside this threshold band when moving away from the point of maximum film thickness to either side is considered as the limit of the uniform pressure zone. a_L and a_R in Figure 24 give the extent of the uniform pressure zone to the left and right of the time of maximum film thickness. The total extent of the uniform pressure zone is denoted as $A = a_L + a_R$. A threshold band that is too small results in inaccurate measurement of the extent uniform pressure zone because of noise in the measurements. However, for threshold bands between 5% and 15% of the peak-to-peak pressure the measured values of A, a_L and a_R are insensitive to the band width.

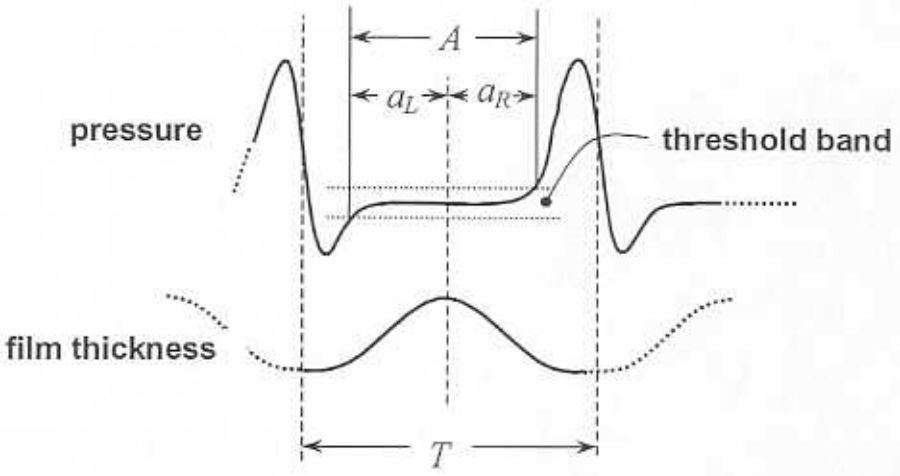

Fig. 24 Determination of the uniform pressure zone extent.

Figure 25 shows typical values of the uniform pressure zone extent normalized with respect to the period of journal motion (T) versus the reference mixture volume fraction, i.e., it provides A, a_L and a_R in terms of the fraction of the period of motion that they cover. The figure shows the results corresponding to the averaged pressure fields at 8.33 Hz (180°, Z_2), which are representative of the measurements at all locations and at the two test operating speeds (8.33 Hz and 16.67 Hz). The threshold band is fixed to 10% of the peak-to-peak pressure amplitude. The vertical bars represent the uncertainty in the measurement of the uniform pressure zone due to the discrete nature of the time domain. It is clear that the uniform pressure zone centers around the location of the maximum film thickness (a_L=a_R). This result applies to all the locations and speeds studied.

Figure 26 shows the average of the uniform pressure zone extent measurements around the damper at two different journal whirl frequencies. The dots represent the spatial average (from transducers at different locations) and the vertical bars include the spatial variation plus the uncertainty due to the discretization of the time scale. The fraction of the period covered by the uniform pressure zone does not change with the operating speed or the location of measurement. It seems to be only a function of the mixture volume fraction, at least for the range of speeds studied. More tests should be performed to corroborate this fact and extend its implications to higher speeds. This is an enterprise worthy to pursue since it will provide a simple way to experimentally quantify the amount of air entrained into a *SFD*.

It appears that the fraction of the journal motion period covered by the uniform pressure zone is independent of the operating speed. Thus, the empirical relation of Figure 26 can be used to estimate the volume fraction by measuring the extent of the uniform pressure zone. Even more, the simple relation $A/T = \beta^2$, depicted with a dashed line in the figure, seems to provide a good approximation that could be useful in engineering applications for β<0.6, which probably covers most practical applications.

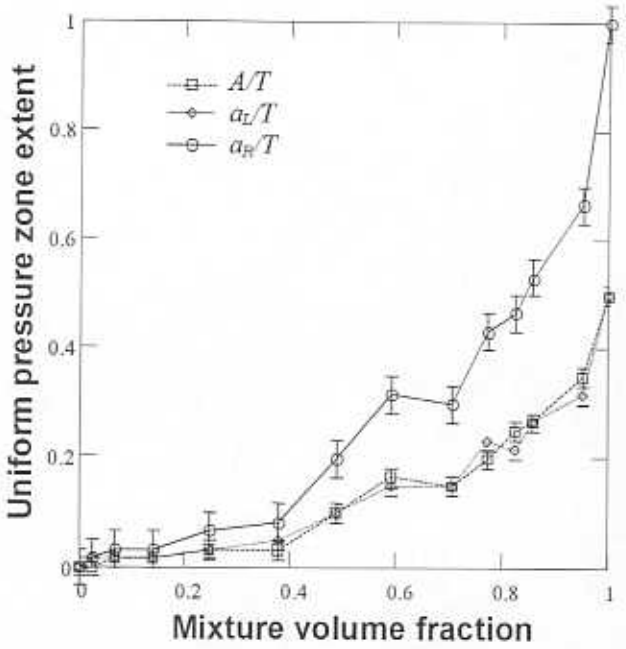

Fig. 25 Extent of the uniform pressure zone versus the mixture volume fraction (typical).Measurements at 8.33 Hz, Z_2, 0°.

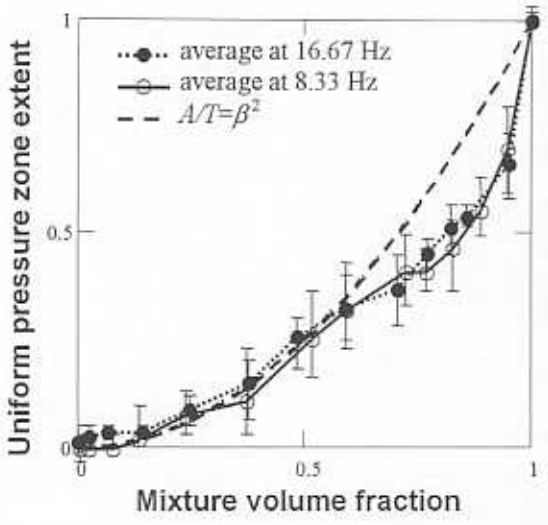

Fig. 26 Averaged extent of the uniform pressure zone versus the mixture volume fraction for whirl frequencies of 8.33 and 16.67 Hz.

4.3 Predicted Forced Response of a *SFD* Operating with Air Entrainment

In this section the theoretical models developed in the previous sections are employed to predict the performance of the test squeeze film damper with free air entrainment. Equation

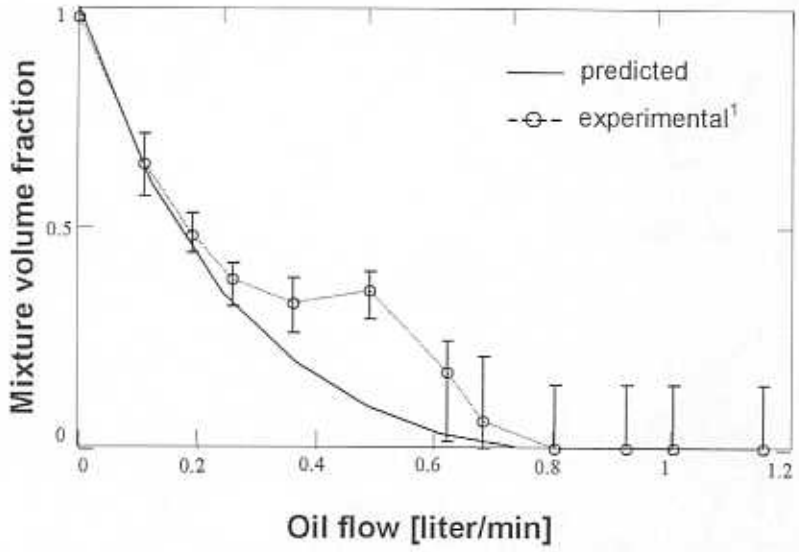

Fig. 27 Reference mixture volume fraction versus oil through flow rate for operation at 8.33 Hz with one open end to ambient.
[1] estimated from measured pressure waves.

(64) is employed to estimate the volume fraction at the reference state (selected as the pressure at the exit plenum). This reference state is then input to the theoretical model to calculate the pressure fields and the hydrodynamic forces.

4.3.1 SFD hydrodynamic pressures and forces versus oil flow rate

The first case studied corresponds to operation at a fixed whirl frequency (ω=8.33 Hz) with variable supply pressure (oil through flow). The test *SFD* is depicted in Figure 2. The journal diameter is D=129.4 mm, the length is L=31.1, and the radial clearance is C=0.343 mm. The average of the measured orbit radius is e=0.18 mm over the whole range of supply pressures studied. The pure oil viscosity at the operating temperature is 77.5 centipoise and its density is 870 kg/m^3. The discharge plenum is full of air at a pressure P_o=1 bar.

Figure 27 shows the predicted reference volume fraction with a continuous line as a function of the oil flow rate. The circles denote the mixture volume fraction estimated from the experimental measurement of the uniform pressure zone extent and using linear interpolation to the relation of Figure 26 ($A/T = f_{(\beta)}$). The vertical bars represent the uncertainty due to the discretization of the time domain. Note that the smaller the volume fraction, the larger the uncertainty. Both predictions and measurements show operation with pure air ($\beta = 0$) when a continuous oil supply is not present ($Q_{oil} = 0$). Also, predictions and measurements show that an oil flow rate of about 0.8 liter/min is enough to prevent air entrainment. Above this value the damper operates with a pure oil lubricant film.

The experimental measurements show a peculiar increase in the volume fraction for oil flow rates between 0.3 and 0.6 liter/min. This is probably related to the measurement procedure implemented for the uniform pressure zone extent. However, since a similar trend is observed, though in a much smaller scale, in the results for peak-to-peak pressures and tangential forces

presented later, no further attempt to tune the estimation of the uniform pressure zone extent is sought.

Figure 28 compiles the computed pressure profiles as a function of time at the axial location Z_2=16.7 mm. An increase in the generation of hydrodynamic pressure is evidenced as the oil flow increases. Note that the film pressure fluctuates about a mean value equal to the discharge plenum pressure. The results also evidence the displacement of the maximum pressure peak towards the point of minimum film thickness as the oil flow rate is decreased (i.e., as the air entrainment increases). Figure 29 shows the theoretical predictions in the same format as for the corresponding experimental pressure profiles (Diaz and San Andrés, 1997). The graph depicts the pressure profiles in a waterfall-like plot, with pressure in the vertical direction, time (angular location) in the horizontal axis, and oil flow rate in the in-plane axis. The uniform pressure zone is outlined according to the experimental observations. The theoretically predicted pressure fields do not reproduce the constant pressure zone identified in the

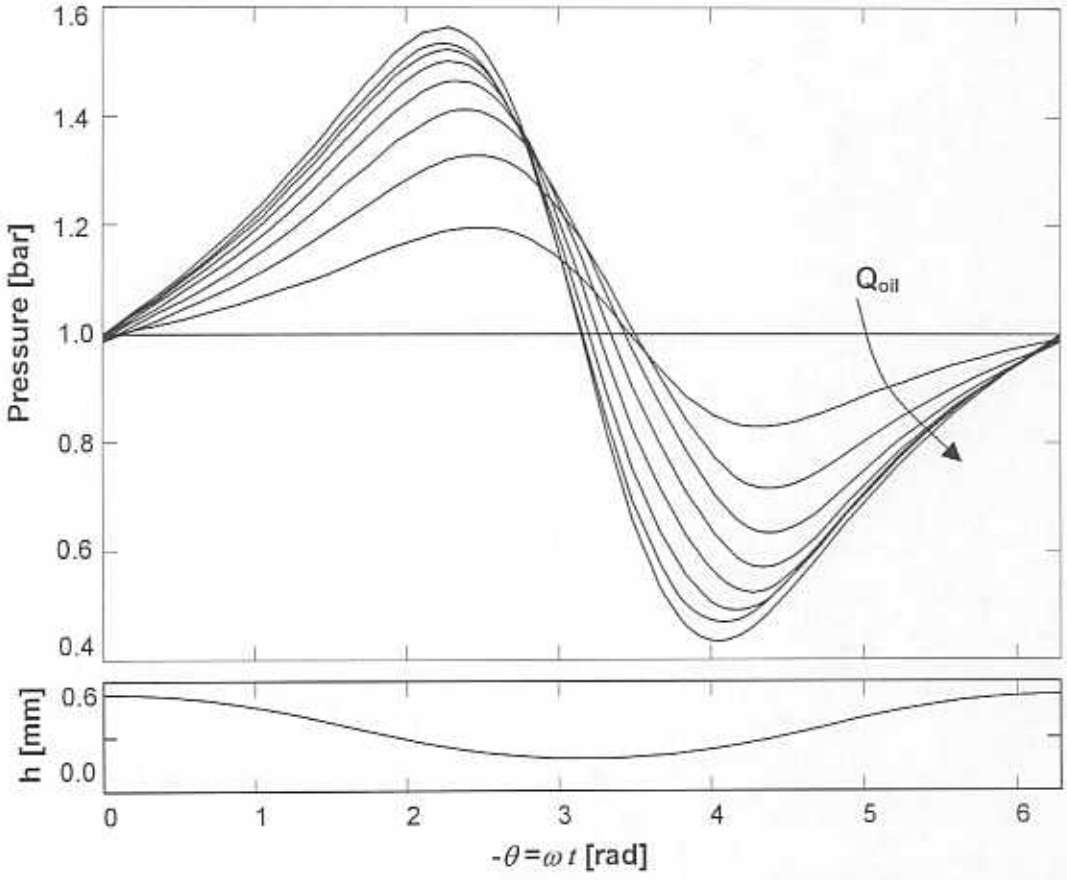

Fig. 28 Predicted pressure profiles for increasing oil through flow rate and operation at 8.33 Hz with one open end to ambient (axial plane Z_2).

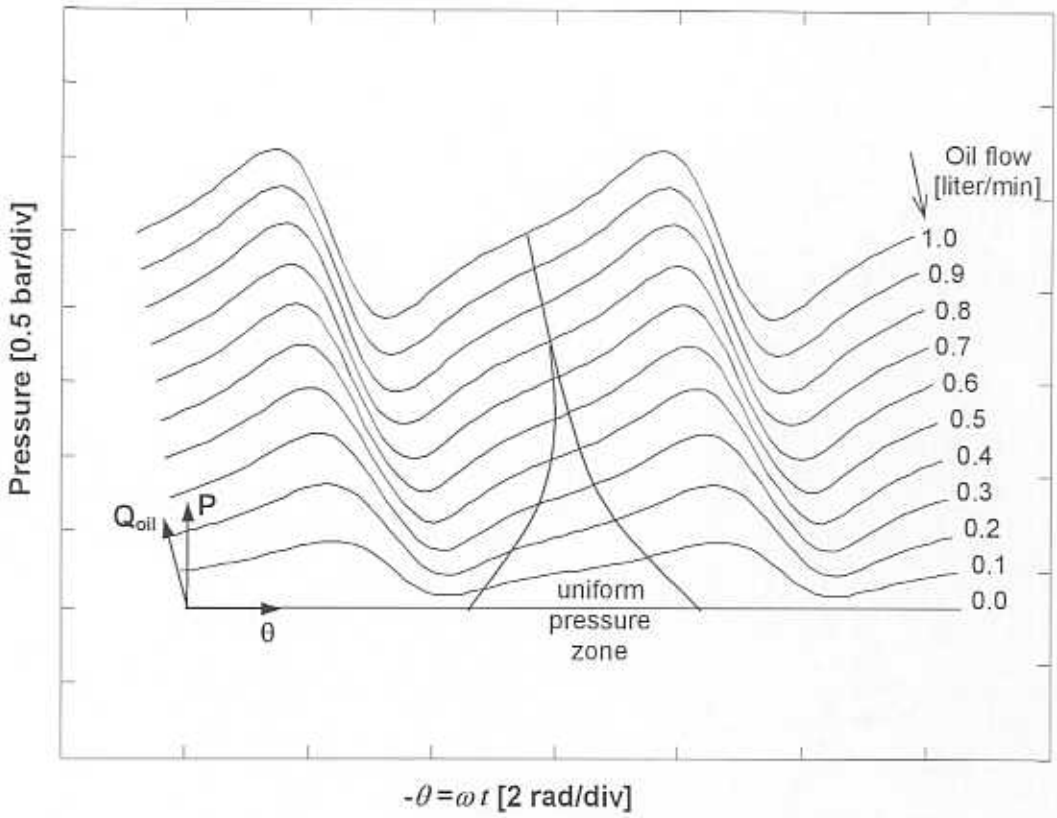

Fig. 29 Development of predicted pressure profiles with the oil through flow rate for operation at 8.33 Hz. One open end to ambient, axial plane Z_2.

experiments. However, in the predicted pressure fields, the zone corresponding to the experimentally determined uniform pressure zone corresponds to an area where the pressure generation is significantly smaller than elsewhere. As previously discussed, further study is required to identify the nature of this zone to improve the analysis.

Figure 30 compiles the peak-to-peak pressure amplitudes as a function of the oil flow rate. The continuous line depicts the predicted values and the dotted line represents the experimental measurements. The vertical bars denote the first order uncertainty from the measurements. The p-p pressure has a nil value for zero oil flow rate and approaches the value corresponding to the incompressible lubricant as the oil flow rates increases. For oil flow rates above 0.8 liter/min, both predictions and measurements show operation with a pure liquid lubricant film, i.e., where the effects of air entrainment have been suppressed. In the range of oil flow rates between 0 and 0.8 liter/min, predictions and measurements show reduced hydrodynamic pressure magnitudes indicating the occurrence of air entrainment. However, the predicted peak-to-peak pressure amplitudes are always lower than the experimentally measured ones.

Figure 31 shows the radial and tangential forces obtained by integration of the measured and predicted pressure fields. Solid lines represent theoretical predictions and dotted lines depict experimental measurements. Squares denote the (-) tangential (damping) force and circles denote the (-) radial (centering) force. The tangential force starts from a zero value, (null

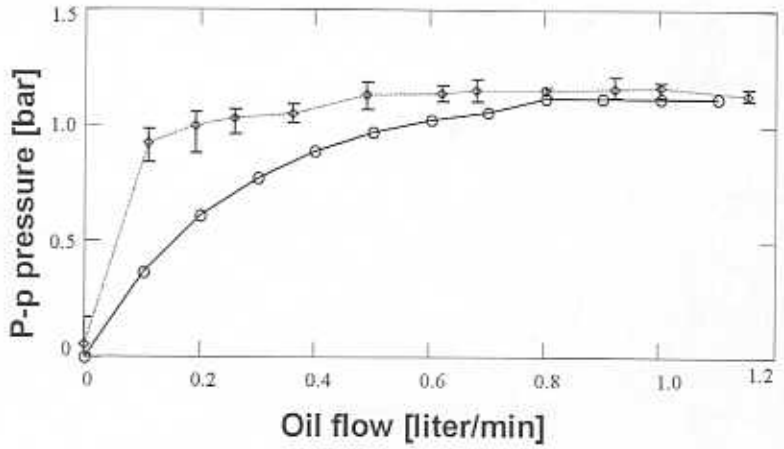

Fig. 30 Peak-to-peak pressure versus oil flow rate for open end to ambient operation at 8.33 Hz.

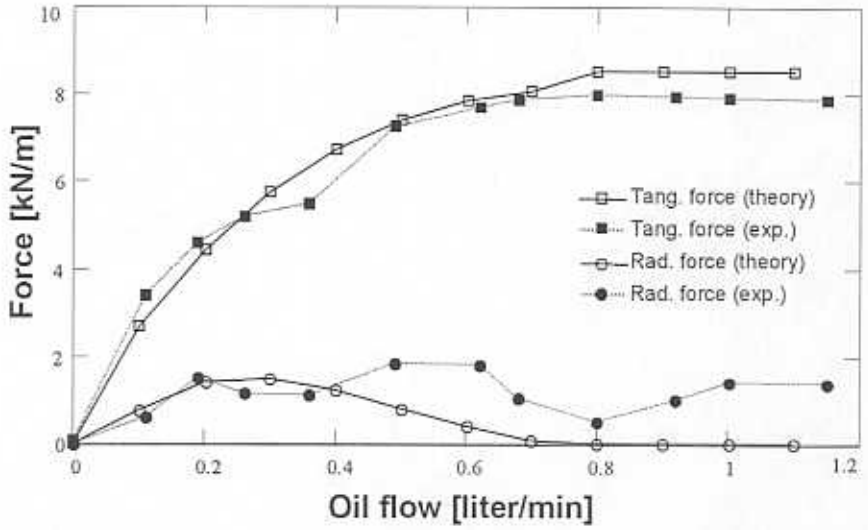

Fig. 31 Predicted radial and tangential forces versus oil through flow rate for operation at 8.33 Hz with one open end to ambient at the axial plane Z_2.

oil flow rate), and increases asymptotically to the value of force corresponding to operation with pure oil as the oil flow rate increases to 0.8 liter/min. The correlation of the analytical predictions of tangential force with the experimental measurements is very good. Yet, the experimentally measured tangential force, as well as the peak-to-peak pressure, present a peculiar behavior for oil flow rate around 0.4 liter/min that seems to resemble the one described for the reference mixture volume fraction.

The predicted radial centering force starts from a null value and increases with the oil flow rate up to about 0.3 liter/min where it reaches a maximum. The radial force decreases slowly

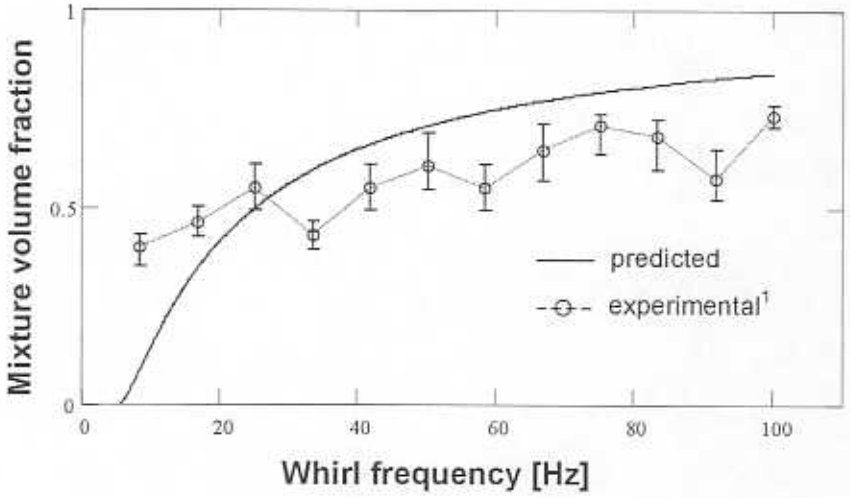

Fig. 32 Reference mixture volume fraction versus whirl frequency for operation with one open end to ambient and oil through flow rate equal to 0.12 liter/min.
[1] estimated from measured pressures

until vanishing for oil flow rates above 0.8 liter/min. The experimental radial force also starts from zero and increases with the oil flow rate in a similar form as in the predictions. Yet, above an oil flow rate of 0.4 liter/min the experimental radial force varies at random and shows different values than those predicted. These random variations may be related to the fact that, when the tangential force is much larger than the radial force, this is highly sensitivity to the journal motion phase angle (which is used to project the total force into the radial and tangential directions). Recall that the experimental journal motion phase angle is estimated by a curve fitting of the local film thickness.

4.3.2 SFD hydrodynamic pressures and forces versus whirl frequency

The second case studied corresponds to operation of the test *SFD* with a constant oil through flow rate of 0.12 liter/min and increasing whirl frequencies to 100 Hz. Recall that the journal diameter is D=129.4 mm, the length is L=31.1, and the radial clearance is C=0.343 mm. The average of the measured orbit radius is e=0.18 mm over the whole range of supply pressures studied. The oil viscosity at the operating temperature is 77.5 centipoise and its density is 870 kg/m^3. The discharge plenum pressure is P_o=1 bar. The experimental results are described in Section 2.

Figure 32 gives the reference mixture volume fraction as a function of the whirl frequency. The continuous line depicts the analytical prediction and the circles denote the estimates based on the measurement of the uniform pressure zone extent on the experimental pressure waves. The vertical bars give the uncertainty in the measurements of the uniform pressure zone extent propagated to the estimated (from the experimental measurements) mixture volume fraction. The experimental and analytical results present satisfactory agreement. The analytical results show that for very small whirl speeds no air entrainment occurs. Unfortunately, there is not test data available below 8.33 Hz to confirm this trend.

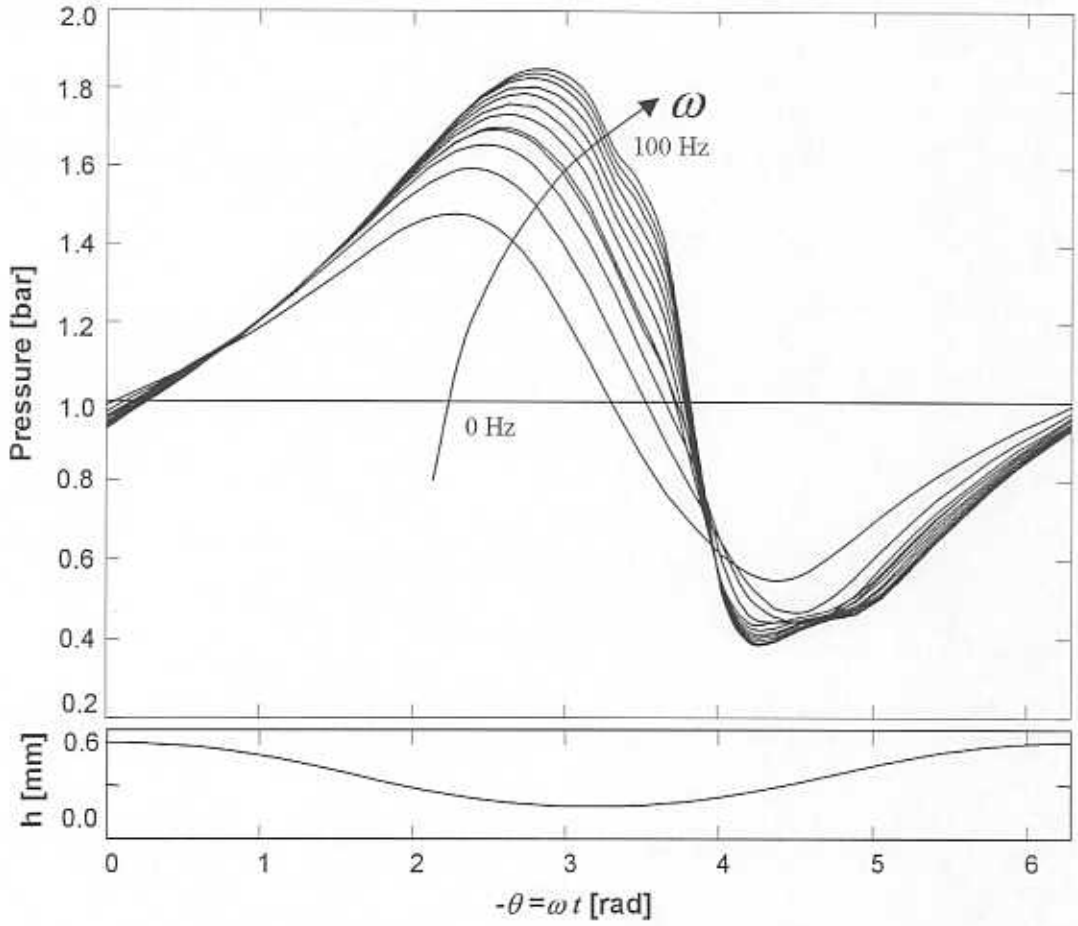

Fig. 33 Predicted pressure profiles for increasing whirl frequency and operation with one open end to ambient, axial plane Z_2 (Q_{out}= 0.12 liter/min).

Figure 33 compiles the predicted pressure fields versus time (angular location) for increasing shaft speed at steps of 500 rpm (8.33 Hz). The magnitude to the maximum peak pressure increases with the journal whirl frequency, while the minimum pressure peak remains of about the same magnitude. The maximum pressure peak moves towards the location of maximum film thickness ($\theta = \pi$) and the transition from the maximum to the minimum pressure peaks becomes steeper. Figure 34 presents the predicted pressure fields in the same format employed for the experimental results shown in Diaz and San Andrés (1997). The pressure and time (angular location) are depicted in the vertical and horizontal axis, respectively. The whirl frequency is represented in the in-plane axis. The area corresponding to the uniform pressure zone identified in the experimental measurements is shown in the figure, but it is clear that the predicted pressure profiles do not reproduce this unique characteristic of the measured pressure profiles.

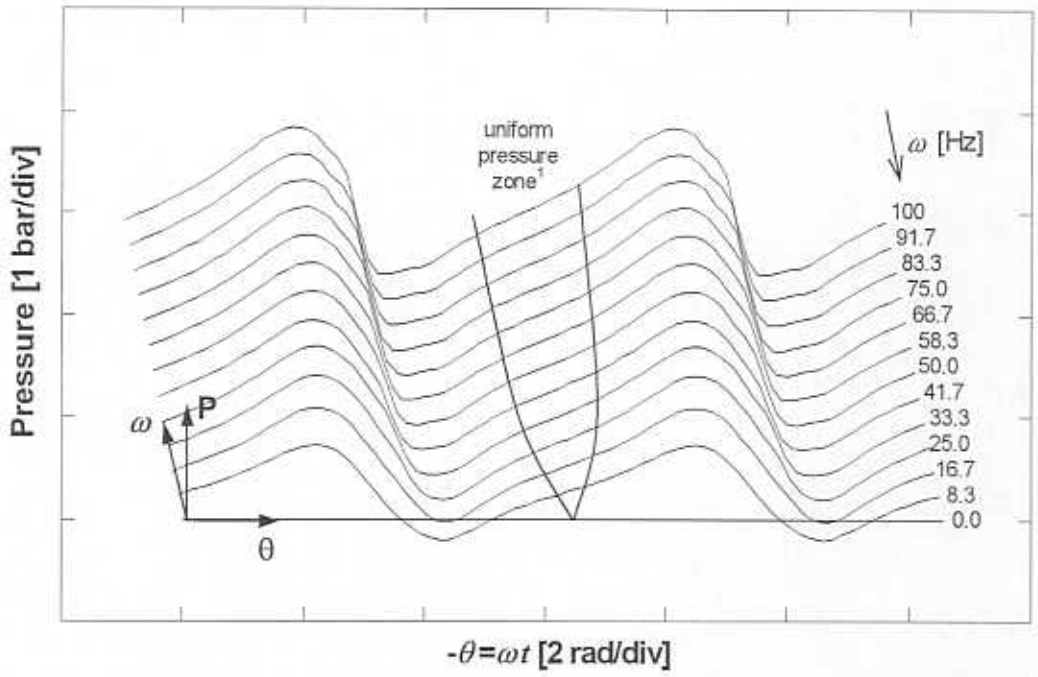

Fig. 34 Development of the predicted pressure profiles with the whirl frequency for operation with one open end to ambient and oil through flow rate equal to 0.12 liter/min. Axial plane Z_2.
[1] uniform pressure zone estimated from experimental pressures

Figure 35 displays the peak-to-peak amplitude of the pressure as a function of the whirl frequency. The continuous line represents the analytical predictions of the hydrodynamic pressure amplitude and the dotted line denotes the experimental values. The vertical bars give the first order uncertainty, or temporal fluctuations, of the experimental measurements. The hydrodynamic pressure generation increases rapidly for small increments of the journal whirl frequency from zero. As the whirl frequency increases, the rate of increment of the peak-to-peak pressure is reduced. Note that classical lubrication theory for incompressible lubricants predicts a linear increase of the peak-to-peak pressure with the whirl frequency. At the maximum whirl frequency studied, the peak-to-peak pressure is still slowly increasing with the whirl frequency. Fair agreement between predicted and measured peak-to-peak pressures is observed.

Figure 36 shows the radial (centering) and tangential (damping) force components per unit length as a function of the whirl frequency. Both forces are obtained from numerical integration of the pressure profiles according to equation (3). Theoretical values are depicted with continuous lines and experimental measurements are represented by dotted lines. Squares denote (-) tangential forces while circles denote (-) radial forces. The predicted tangential forces show a similar behavior to that of the peak-to-peak pressures. However, the measured tangential force increases only for small whirl frequencies and monotonically decreases for whirl frequencies above 20 Hz. Good agreement between theory and experiments is achieved for small whirl frequencies, but above 20 Hz the predictions diverge from the measurements predicting a tangential force of approximately 2.5 times the measured value for a whirl frequency of 100 Hz. The radial (centering) force increases monotonically with the whirl

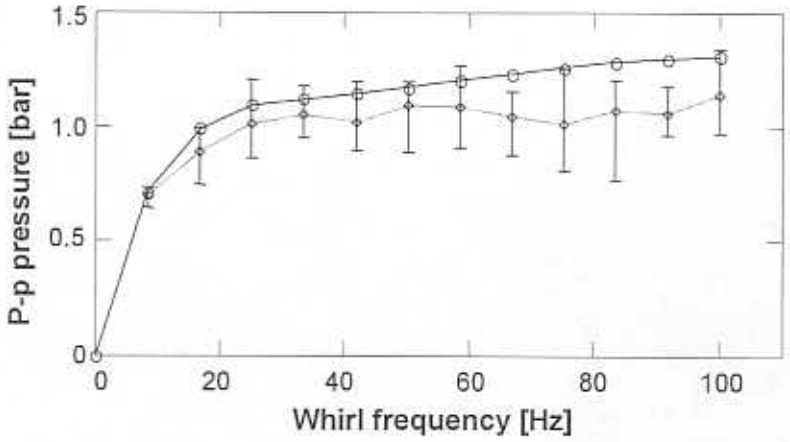

Fig. 35 Peak-to-peak pressure versus whirl frequency for operation with one open end to ambient and oil through flow rate equal to 0.12 liter/min. Axial plane Z_2.

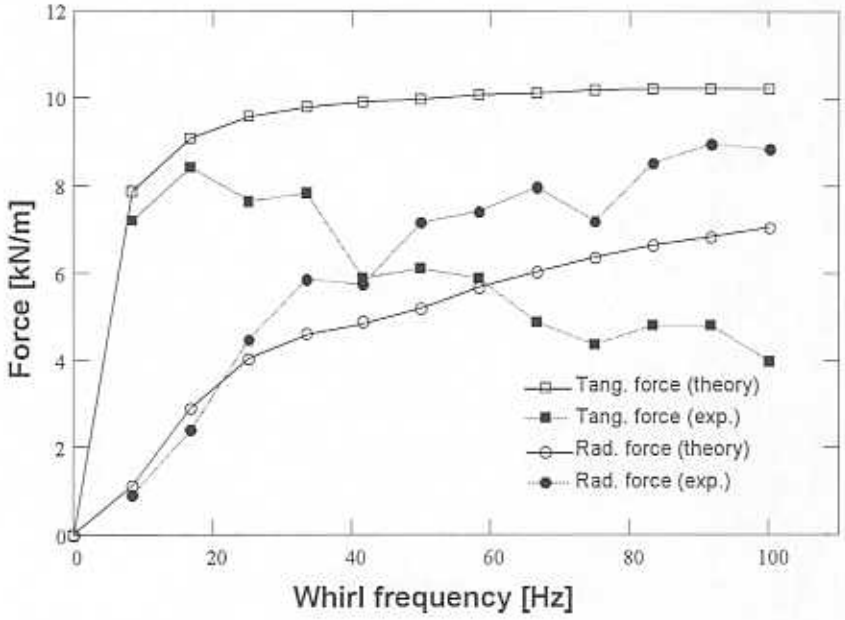

Fig. 36 Radial and tangential forces per unit length versus whirl frequency for operation with one open end to ambient and oil through flow rate equal to 0.12 liter/min. Axial plane Z_2.

frequency. The predicted radial force presents fair agreement with the experimentally derived values, though the difference between predictions and measurements is large for the higher whirl frequencies.

Figure 37 provides an alternative representation of the hydrodynamic force in terms of its total magnitude and the angle with the radial direction. For low speeds the model predictions render very good agreement with the measurements. As the whirl frequency increases, the total

force is still satisfactorily predicted. Both, measured and predicted total force follow the same trend of the peak-to-peak pressures, increasing rapidly for low whirl frequencies and progressively slower as the whirl frequency increases. The force starts as a purely tangential (damping) force for whirl frequency close to zero, but it rapidly departs from the tangential direction as the frequency increases. The model predictions follow the measurements up to a whirl frequency of 20 Hz. Yet, for higher whirl frequencies the measured force displaces faster towards the radial direction than the model predictions. This difference could be related to the occurrence of the uniform pressure zone, which the model is unable to predict. Thus, further research to include this effect is desirable.

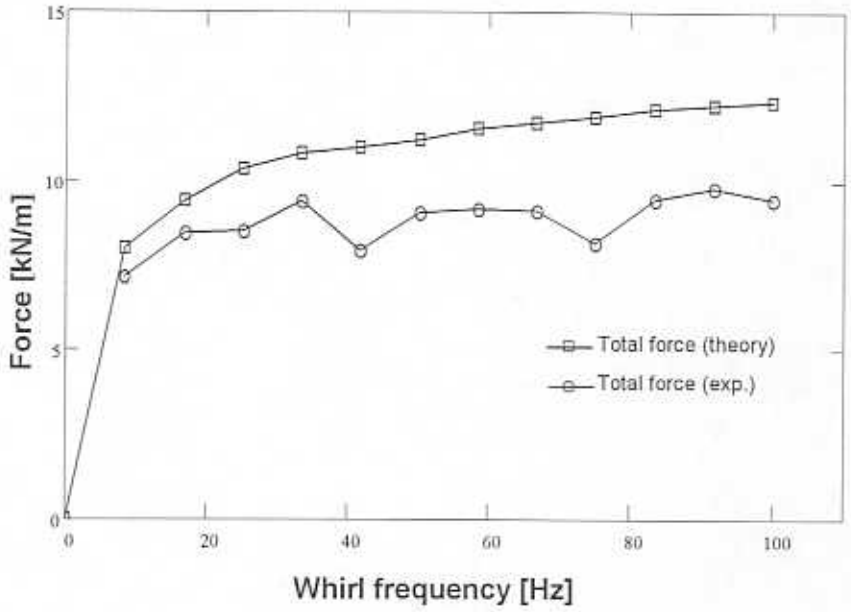

(a) Magnitude.

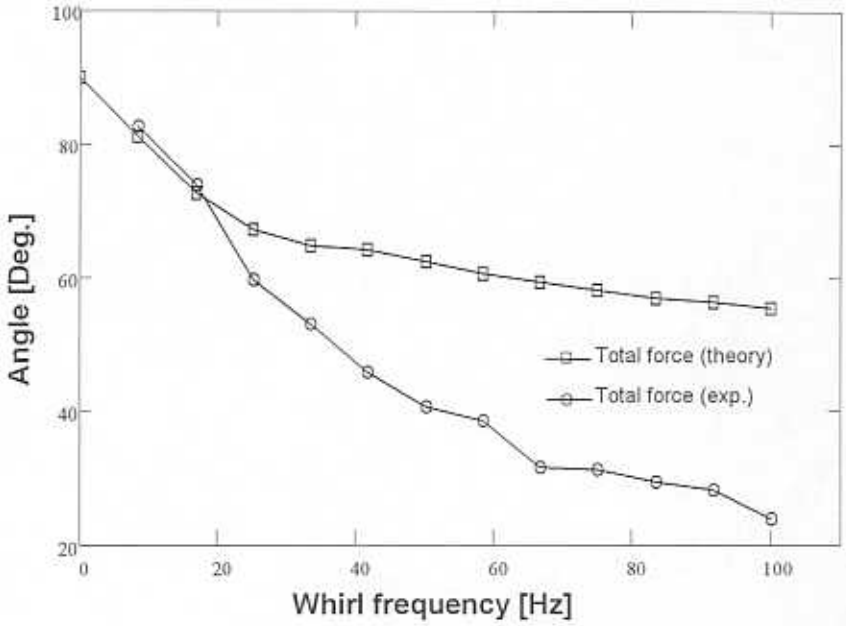

(b) angle from the radial direction.

Fig. 37 Total force versus whirl frequency for operation with one open end to ambient and oil through flow rate equal to 0.12 liter/min.

5. CONCLUSIONS AND RECOMMENDATIONS

Most squeeze film dampers in practice show the phenomenon of air entrapment. It is generally accepted that the presence of air reduces the damping capability of the *SFD*, especially at large amplitudes and high frequencies of vibration. At a first glance, this may seem a serious problem whose obvious solution points out to an increase in the oil flow rate. Yet, the cost and bulky equipment required to insure that no air enters the film renders this option impractical. Furthermore, years of practice have demonstrated that *SFDs* are able to generate the required damping even when operating with air entrapment. Indeed, it is speculated that the reduction of damping at high frequencies is beneficial in rotor-bearing systems operating at supercritical speeds. Thus, it has been imperative for some time the definition of a reliable model to allow for the analysis and design of *SFDs* operating with air entrapment, by far the most common operating condition and –at the same time– the less understood of them all. The present research presents an important contribution towards this direction, by providing a novel compilation of experimental and theoretical analyses on the subject.

A comprehensive experimental study of the operation of squeeze film dampers with air entrapment (both freely entrained and forced into the lubricant) is presented. The experimental results advance the state of the art in the current knowledge of the phenomenon by comparing –for the first time– the performance of a *SFD* with freely entrained air and that of a *SFD* operating with a controlled bubbly mixture. The experiments show that both operating conditions lead to a dynamic force performance that deviates considerably from the operation without air entrainment (with or without lubricant vapor cavitation). Therefore, all models currently available (and based on the assumption that the lubricant does not contain air) render predictions that are, at most, of reduced practical use for the analysis of *SFDs*.

It is qualitatively established that both regimes (freely entrained air and operation with a controlled bubbly mixture) lead to the same type of pressure profiles. This fact bolsters the possibility of devising mathematical models based on the operation with bubbly mixtures to predict the performance of a damper with natural air entrainment. The experiments with controlled bubbly mixtures provide quantitative description of different characteristics of the phenomena, and including the reduction of hydrodynamic pressures and forces with the amount of air present in the lubricant, the occurrence of a uniform pressure zone whose extent is proportional to the mixture air volume fraction, the shift from a tangential (damping) force to a radial (stiffness-like) force as the air entrapment increases, etc. Thus, a reliable data base to benchmark the performance of theoretical models has been made available.

A mathematical model considering the lubricant as a *homogeneous* mixture of air bubbles finely dispersed within an oil matrix is developed. The air is modeled as an ideal gas while the oil is regarded as an incompressible fluid. The homogeneity assumption –which means that the two components of the mixture are so well mixed that no relative motion occurs– seems to be confirmed by the experiments. Under these conditions, the averaged momentum and continuity equations for both components are combined to obtain a single generalized Reynolds equation for the damper film pressure in which the mixture is represented by effective properties. Dukler's correlation is employed to estimate the mixture effective viscosity. A simplified form of the Rayleigh-Plesset differential equation –which describes the bubble size as a function of the pressure of the liquid surrounding it– is introduced to estimate the mixture air volume fraction (and thus its effective density) as a function of the local pressure. Further

simplification is attained by assuming the bubbles in quasi-static equilibrium and by adopting the infinitely short length model assumptions. The resulting model comprises a differential equation for the pressure (the Reynolds equation) coupled to two algebraic equations for the effective mixture properties (Dukler's viscosity correlation and the quasi-static Rayeigh-Plesset equation). The amount of air entrapped is specified by fixing the air/oil mass ratio in the form of a reference volume fraction at certain given mixture conditions.

Comparison of the model predictions with the experimental results for controlled bubbly mixtures is promising and the model already provides results of immediate engineering applicability. Yet, some refinements are required to address certain phenomena that the present model is unable to predict.

Among these unpredicted phenomena the most relevant is the occurrence of the uniform pressure zone around the point of maximum film thickness. It is speculated that this constant pressure zone can be related either to the presence of a large bubble moving synchronously with the journal whirl, or to unstable growth of the bubbles under certain conditions (low pressure or large bubble radii). To consider unstable growth of the bubbles, the dynamic terms of the Rayleigh-Plesset equation should be retained in the analysis and the resulting model would require the simultaneous solution of two coupled differential equations. To consider a single large bubble (or group of bubbles) moving around the damper synchronously with the journal whirl motion, a set of boundary conditions similar to those applied for vapor or single bubble gaseous cavitation should be implemented into the model hereby developed. It is anticipated that both approaches could render similar results since the set of boundary conditions could be identified as defining the zone in which the bubbles are unstable. The introduction of boundary conditions seems easier to implement numerically into the solution. Yet, the definition of adequate and physically sound boundary conditions may not be an easy task. Another important factor not predicted by the present model is related to the hydrostatic pressure field given by the axial through flow. In most practical cases the through flow is small and the hydrostatic pressure is not relevant. Yet, it is expected that consideration of the axial flow would render forces even closer to those measured in the current experiments –where the axial flow is unusually large– thus improving the predictions to measurements correlation. This can be easily achieved by specifying the through flow as a boundary condition on the damper sealed end.

In addition, a simple model based on the balance of mass in the axial direction is presented for estimation of the amount of air trapped within the film. This model neglects the circumferential flow (as it is done in the infinitely short length model) and uses an average density for the air. Time averaged flow rates are obtained by integration over one period of journal motion. Then, assuming that the lubricant and air within the film are uniformly mixed, a reference mixture air volume fraction is computed as the ratio of the averaged air flow entering the film to the averaged total flow (air+oil) entering the damper lands. The reference mixture air volume fraction (β_o) is written as a function of a single dimensionless parameter hereby introduced. This dimensionless parameter represents the ratio of the oil flow supplied to the damper and the flow required to completely fill the growing film volume (given by the maximum rate of volume change). For a *SFD* executing circular center orbits, the dimensionless parameter depends on the physical parameters: oil through flow rate, journal length and diameter, and whirl orbit radius and frequency. This means, as experiments and previous investigators suggest, that the severity of air entrainment is related to the particular damper geometry, characteristics of the journal motion, and the supply flow rate (or supply

pressure). Lower oil flow rates (lower supply pressures), larger amplitudes of motion or higher speeds all translate into increased air entrainment.

An empirical correlation between the amount of air present in the lubricant mixture (expressed in terms of the reference mixture air volume fraction, β_o) and the extent of the uniform pressure zone is constructed using the experimental data from the tests with controlled mixtures. Thus, an empirical formula to estimate experimentally the volume of air trapped within the damper is made available. The air volume fraction in the experiments with freely entrained air is estimated using this empirical correlation and the results compare extremely well with those predicted by the analytical model. Furthermore, the theoretical model for estimation of the reference volume fraction is combined with the quasi-static homogeneous bubbly mixture model for the computation of the pressure field. The predictions of this combined model are compared to experimental measurements of the performance of the test *SFD* operating with freely entrained air at different speeds and supply pressures. The good correlation between predictions and measurements reinforces the possibility of using this model for practical applications in *SFDs* design and analysis. However, the assumption of negligible circumferential flow and the use of an average density for the air limit the applicability of the analytical model for the estimation of β_o. Yet, these assumptions are only used to estimate local axial flows. It seems plausible to use a similar approach to define the reference air volume fraction using flow rates numerically calculated from the solution of the bubbly mixture *SFD* model.

REFERENCES

Braun, M. J. and Hendricks, R. C., 1984, "An Experimental Investigation of the Vaporous/Gaseous Cavity Characteristics of an Eccentric Journal Bearing," *ASLE Transactions*, Vol. 27, 1, pp. 1-14.

Brennen, C. E., 1995, *Cavitation and Bubble Dynamics*, Oxford Engineering Series 44, Oxford University Press, New York.

Chamniprasart, K., Al-Sharif, A., Rajagopal, K.R., and Szeri, A. Z., 1993, "Lubrication with Binary Mixtures: Bubbly Oil," *ASME* Journal of Tribology, Vol. 115, pp. 253 - 260.

Childs, D., 1993, *Turbomachinery Rotordynamics*, John Wiley & Sons, New York.

Diaz, S., 1996, "Measurements of Pressure in a Squeeze Film Damper with a Bubbly Mixture," TAMU Turbomachinery Research Consortium Progress Report, TRC-SFD-1-96, College Station, TX, May.

Diaz, S. E., 1999, "The Effect of Air Entrapment on the Performance of Squeeze Film Dampers: Experiments and Analysis," Ph.D. Dissertation, Texas A&M University, College Station, TX, May.

Diaz, S. E., and San Andrés, L. A., 1997, "Forced Response of *SFD*s Operating with a Bubbly (Air/Oil) Mixture," TAMU Turbomachinery Research Consortium Progress Report, TRC-*SFD*-1-97, College Station, TX, April.

Diaz, S. E., and San Andrés, L. A., 1998a, "Measurements of Pressure in a Squeeze Film Damper with an Air/Oil Bubbly Mixture," *STLE Tribology Transactions*, Vol. 41, 2, pp. 282-288.

Diaz, S. E., and San Andrés, L. A., 1998b, "Reduction of the Dynamic Load Capacity in a Squeeze Film Damper Operating with a Bubbly Lubricant," *ASME* Paper 98-GT-109.

Diaz, S. E., and San Andrés, L. A., 1998c, "Effects of Bubbly Flow on the Dynamic Pressure Fields of a Test Squeeze Film Damper," *ASME* Paper FEDSM98-5070, *Proceedings of the 1998 ASME Fluids Engineering Division Summer Meeting*, Washington, DC, June.

Diaz, S., and L. San Andrés, 1999, "Air Entrainment vs. Lubricant Vaporization in Squeeze Film Dampers," *ASME* Paper 99-GT-187, accepted for presentation at *ASME* Turbo Expo'99, Indianapolis, June, and publication at *ASME* Journal of Gas Turbines and Power, June.

Dowson, D., and Taylor, C. M., 1979, "Cavitation in Bearings," *Ann. Rev. Fluid Mechanics*, Vol. 11, pp. 35-61.

Einstein, A., 1906, "Eine neue Bestimmung der Molekul-Dimension," ("*A New Approach to the Molecular Dimension*") Ann. Physik, Vol. 19, p. 289-297.

Feng, N.S., and Hahn, E. J., 1986, "Density and Viscosity Models for Two-Phase Homogeneous Hydrodynamic Damper Fluids," *ASLE Transactions*, Vol. 29, No. 3, p. 361-369.

Hayward, A. T., 1961, "The Viscosity of Bubbly Oil," N.E.L. Fluids Report No. 99, National Engineering Laboratory, London, UK.

Hibner, D., and Bansal, P., 1979, "Effects of Fluid Compressibility on Viscous Damper Characteristics," *Proceedings of the Conference on the Stability and Dynamic Response of Rotors with Squeeze Film Bearings*, University of Virginia, pp. 116-132.

Jacobson, B. O., and Hamrock, B. J., 1983, "High-Speed Motion-Picture Camera Experiments of Cavitation in Dynamically Loaded Journal Bearings," *ASME* Journal of Lubrication Technology, Vol. 1, July, pp. 446-452.

Jung, S. Y., and Vance, J. M., 1993a, "Effects of Vapor Cavitation and Fluid Inertia on the Force of a Squeeze Film Damper Part I - Analysis of a Long *SFD*," *STLE Tribology Transactions*, Vol. 36, No. 4, pp. 597-604.

Jung, S. Y., and Vance, J. M., 1993b, "Effects of Vapor Cavitation and Fluid Inertia on the Force of a Squeeze Film Damper Part II - Experimental Comparisons," *STLE Tribology Transactions*, Vol. 36, No. 4, pp. 700-706.

Kline, S. J., and McClintock, F.A., 1953, "Describing Uncertainties in Single-Sample Experiments," *ASME* Mechanical Engineering, Vol. 75. pp. 3-8.

Ku, C. P., and Tichy, J. A., 1990, "An Experimental and Theoretical Study of Cavitation in a Finite Submerged Squeeze Film Damper," *ASME* Journal of Tribology, Vol. 112, pp. 725-733.

Moffat, R. J., 1982, "Contributions to the Theory of Single-Sample Uncertainty Analysis," *ASME* Journal of Fluids Engineering, Vol. 104, pp.250-260.

Pinkus, O., 1990, *Thermal Aspects of Fluid Film Tribology*, *ASME* Press, New York, pp. 317-326.

Schlichting, H., 1955, *Boundary Layer Theory*, McGraw-Hill, New York, pp. 117-123.

Sun, D. C., and Brewe, D. E., 1992, "Two Reference Time Scales for Studying the Dynamic Cavitation of Liquid Films," *ASME* Journal of Tribology, Vol. 114, pp. 612-615.

Sun, D. C., Brewe, D. E., and Abel, P.B., 1993, "Simultaneous Pressure Measurement and High-Speed Photography Study of Cavitation in a Dynamically Loaded Journal Bearing," *ASME* Journal of Tribology, Vol. 115, pp. 88-95.

Szeri, A.Z., 1980, *Tribology: Friction, Lubrication, and Wear*, McGraw-Hill, New York.

Szeri, A. Z., 1996, "On the Flow of Emulsions in Tribological Contacts", *Wear*, Vol. 200, pp.353-364.

Tao, L., Diaz, S., San Andrés, L., and Rajagopal, K., 1998, "Flow Analysis of Squeeze Film Dampers Operating with Bubbly Lubricants," TAMU Turbomachinery Research Consortium Progress Report, TRC-SFD-1-98, College Station, TX.

Taylor, G. I., 1932, "The Viscosity of a Fluid Containing Small Drops of Another Fluid," *Proc. Roy. Soc.*, Series A138, pp. 41-49.

Vance, J. M., 1988, "Rotordynamics of Turbomachinery," John Wiley & Sons, New York.

Walton, J., Walowit, E., Zorzi, E., and Schrand, J., 1987, "Experimental Observation of Cavitating Squeeze Film Dampers," *ASME* Journal of Tribology, 109, pp. 290-295.

Zeidan, F. Y., and Vance, J. M., 1989a, "Experimental Investigation of Cavitation Effects on the Squeeze Film Force Coefficients", Rotating Machinery Dynamics, DE-vol. 18-1, *ASME* Conference on Mechanical Vibration and Noise, pp. 237-242.

Zeidan, F. Y., and Vance, J. M., 1989b, "Cavitation Leading to a Two Phase Fluid in a Squeeze Film Damper," *STLE Tribology Transactions*, Vol. 32, 1, pp. 100-104.

Zeidan, F. Y., and Vance, J. M., 1990a, "A Density Correlation for a Two-Phase Lubricant and Its Effect on the Pressure Distribution," *STLE Tribology Transactions*, Vol. 33, pp. 641 - 647.

Zeidan, F. Y., and Vance, J. M., 1990b, "Cavitation Regimes in Squeeze Film Dampers and Their Effect on the Pressure Distribution," *STLE Tribology Transactions*, Vol. 33, pp.447-453.

Zeidan, F. Y., and Vance, J. M., 1990c, "Cavitation and Air Entrainment Effects on the Response of Squeeze Film Supported Rotors," *ASME* Journal of Tribology, Vol. 112, pp. 347 - 353.

Zeidan, F. Y., Vance, J. M., and San Andrés, L. A., 1996 "Design and Application of Squeeze Film Dampers in Rotating Machinery", *Proceedings of the 25th Turbomachinery Symposium*, Texas A&M University, College Station, TX, pp. 169-188.